

# Discovery of Metastable He I\* $\lambda 10830$ Mini-broad Absorption Lines and Very Narrow Paschen $\alpha$ Emission Lines in the ULIRG Quasar IRAS F11119+3257

Xiang Pan<sup>1</sup>, Hongyan Zhou<sup>1,2</sup>, Wenjuan Liu<sup>3</sup>, Bo Liu<sup>2,1</sup>, Tuo Ji<sup>1</sup>, Xiheng Shi<sup>1</sup>, Shaohua Zhang<sup>1</sup>, Peng Jiang<sup>1</sup>, Huiyuan Wang<sup>2</sup>, Lei Hao<sup>4</sup>

## ABSTRACT

IRAS F11119+3257 is a quasar-dominated Ultra-Luminous InfraRed Galaxy, with a partially obscured narrow-line seyfert 1 nucleus. In this paper, we present the NIR spectroscopy of F11119+3257, in which we find unusual Paschen emission lines, and metastable He I\*  $\lambda 10830\text{\AA}$  absorption associated with the previously reported atomic sodium and molecular OH mini-BAL (Broad Absorption Line) outflow. Photo-ionization diagnosis confirms previous findings that the outflows are at kilo-parsec scales. Such large-scale outflows should produce emission lines. We indeed find that high-ionization emission lines ([O III], [Ne III], and [Ne V]) are dominated by blueshifted components at similar speeds to the mini-BALs. The blueshifted components are also detected in some low-ionization emission lines, such as [O II]  $\lambda 3727$  and some Balmer lines ( $H\alpha$ ,  $H\beta$ , and  $H\gamma$ ), even though their cores are dominated by narrow ( $FWHM_{\text{NEL}} = 570 \pm 40 \text{ km s}^{-1}$ ) or broad components at the systemic redshift of  $z = 0.18966 \pm 0.00006$ . The mass flow rate ( $230\text{--}730 M_{\odot} \text{ yr}^{-1}$ ) and the kinetic luminosity ( $\dot{E}_k \sim 10^{43.6\text{--}44.8} \text{ erg s}^{-1}$ ) are then inferred jointly from the blueshifted emission and absorption lines. In the NIR spectrum of F11119+3257, we also find that the Paschen emission lines are unique, in which a very narrow ( $FWHM = 260 \pm 20 \text{ km s}^{-1}$ ) component is shown in only Pa $\alpha$ . This narrow component most probably comes from heavily obscured star formation. Based on the Pa $\alpha$  and Pa $\beta$  emissions, we obtain an extinction at the  $H$  band,  $A_H > 2.1$  (or a reddening of  $E_{B-V} > 3.7$ ), and a star formation rate of  $SFR > 130 M_{\odot} \text{ yr}^{-1}$  that resembles the estimates inferred from the FIR emissions ( $SFR_{\text{FIR}} = 190 \pm 90 M_{\odot} \text{ yr}^{-1}$ ).

*Subject headings:* galaxies: evolution – galaxies: absorption lines – galaxies: emission lines – Galaxies: individual (IRAS F11119+3257)

## 1. INTRODUCTION

Through decades of studies of local galaxies, the tight correlation between the mass of the central black holes and the velocity dispersion of the galaxy bulges (the so-called  $M - \sigma$  relation) is established, which indicates close relation between super-massive black holes (SMBHs) and their host galaxies (Ferrarese & Merritt 2000; Kormendy & Ho 2013). On the other hand, observational evidences of quasar feedback

<sup>1</sup>SOA Key Laboratory for Polar Science, Polar Research Institute of China, 451 Jinqiao Road, Shanghai, 200136, China; zhouhongyan@pric.org.cn

<sup>2</sup>Key Laboratory for Researches in Galaxies and Cosmology, Department of Astronomy, University of Sciences and Technology of China, Chinese Academy of Sciences, Hefei, Anhui, 230026, China; mtzhou@ustc.edu.cn, sidpx@mail.ustc.edu.cn

<sup>3</sup>Yunnan Observatories, Chinese Academy of Sciences, Kunming, Yunnan 650011, China

<sup>4</sup>Shanghai Astronomical Observatory, Chinese Academy of Sciences, Shanghai 200030, China

have been found (see Fabian 2012 for a detailed review). Both analytical models (Scannapieco & Oh 2004) and numerical simulations (Sijacki et al. 2007) discovered that quasar feedback is an important ingredient for regulating galaxy formation, which could lead to the close correlation between SMBHs and their host galaxies.

As one of the key components of quasar feedback, outflows are found in many quasars. Mildly relativistic FeK absorption lines (ultra-fast outflows, or UFOs) are detected in at least  $\sim 35\%$  of the radio quiet AGNs, which are regarded as evidences of AGN accretion disk winds (Tombesi et al. 2010). On the other hand, fast massive OH outflows (maximum speed  $\gtrsim 1000 \text{ km s}^{-1}$ ) are detected in  $\sim 1/3$  of the nearby galaxy mergers with *Herschel* (Veilleux et al. 2013). By comparing the energetics of the UFOs/(disk winds) and the massive molecular outflows, Tombesi et al (2015) argues that energy-conserving mechanism is the basis of the quasar outflow feedback. In addition to the extremely-ionized FeK absorption line in the X-ray band and the molecular absorption lines in the FIR, there are copious broad absorption line (BAL) species in the UV-optical spectrum of BAL quasars. Some high-ionization absorption lines like O VI , N V , C IV doublets are nearly universal in BAL quasars, while Al III , Al II , Mg II and Fe II lines are only significant in Low-ionization BALs (LoBALs). The metastable He I\* absorption, on the other hand, are found to be prevalent in Mg II BALs (Liu et al. 2015). And associated atomic broad absorption lines like Na I are also reported (e.g. Liu et al. 2016). LoBALs generally trace relatively thick or dense outflow clouds, whose physical scale can extend to several kilo-parsecs (e.g. Chamberlain & Arav 2015), i.e. could pose strong feedback to the host galaxies.

Sample studies have found that quasar emission lines are generally asymmetric and blueshifted, e.g. in C IV (Richards et al. 2011; Wang et al. 2011) and in [O III] , [N II] , [S II] , etc (Komossa et al. 2008; Zhang et al. 2011). On the other hand, high-ionization BELs in the SDSS quasar composite spectrum (Vanden Berk et al. 2001) are generally blueshifted as compared to low-ionization lines. These are usually referred to as signs of emission-line outflows. In the meantime, blueshifted emission-line outflows are found to be associated with LoBALs in some quasars (e.g. Rupke et al. 2013; Liu et al. 2016). By analysing blueshifted absorption and emission lines, some properties of the outflow material can be obtained: 1) physical conditions like position, density, and energetics (Sun et al. 2017); 2) geometry (Greene et al. 2012); 3) abundances and chemistry (Dunn et al. 2010). These allow us to probe the driving mechanism of quasar outflows and the strength of outflow feedback to their host galaxies.

IRAS F11119+3257 is a ULIRG ( $L_{\text{IR}} = 10^{12.58} L_{\odot}$ , Kim & Sanders 1998), and a quasar, or more specifically a partially obscured narrow-line Seyfert 1 (NLS1) galaxy ( $\text{FWHM}_{\text{H}\beta} = 1980 \text{ km s}^{-1}$ ; Komossa et al. 2006) in local universe at  $z = 0.18966 \pm 0.00006$ . It is the key object in Tombesi et al (2015), where both a UFO and a molecular outflow are detected. Thus F11119+3257 is a perfect laboratory for studying physical properties of AGN outflows. In this paper, we report a detailed analysis of the blueshifted ionic/atomic absorption and emission lines in the optical-IR spectrum of F11119+3257. The detection of these lines helps in constraining physical properties of the massive molecular outflow. In the meantime, heavily obscured star formation activity in the host galaxy are probed using IR Hydrogen emission lines and PAH/FIR emissions. The connection of the star formation with the galactic-scale outflow is then discussed. Throughout the paper, all uncertainties are at the  $1\text{-}\sigma$  level if not stated specifically. We adopt the standard  $\Lambda$ CDM model with  $H_0 = 70 \text{ km s}^{-1} \text{ Mpc}^{-1}$ ,  $\Omega_{\text{M}} = 0.3$ , and  $\Omega_{\Lambda} = 0.7$ .

## 2. OBSERVATION AND DATA REDUCTION

Photometric and spectroscopic data of F11119+3257 are tabulated in Table 1. Photometric data from optical (SDSS, York et al. 2000) and IR (the Two Micron All Sky Survey, or 2MASS, Skrutskie et al. 2006; Wide-field Infrared Survey Explorer, or *WISE*, Wright et al. 2010) bands are collected to study the Spectral Energy Distribution (SED) of F11119+3257. Multi-epoch photometries are also checked and no significant variability is discovered. Catalina Sky Survey<sup>1</sup> (Drake et al. 2009; ID: CSS\_J111438.9+324133) *V*-band magnitude varied at a level of  $\sim 0.08$  mag between 2005 May 5 and 2013 Jun 7, PTF (Palomar Transient Factory; Law et al. 2009) magnitude varied at a level of  $\sim 0.04$  mag between 2013 Jan 13 and 2014 Apr 04, both of the magnitude fluctuations are consistent with their measurement uncertainties. And no intra-night variability in the infrared is found during *WISE* observations. The IRAS (The Infrared Astronomical Satellite) photometries at  $30\mu\text{m}$ ,  $60\mu\text{m}$ , and  $100\mu\text{m}$  (Moshir & et al. 1990), and the SCUBA photometry at  $850\mu\text{m}$  (Clements et al. 2010) of F11119+3257 are collected to study cold dust emission and star formation activity of the host galaxy. The radio emission of F11119+3257 is detected by the VLA Faint Images of the Radio Sky at Twenty-Centimeters Survey (FIRST; White et al. 1997). With a radio index of  $R_{1.4} = 20$ , F11119+3257 can be referred to as “radio intermediate” (Komossa et al. 2006).

There are a number of archival spectroscopic observations of F11119+3257, which are also summarized in Table 1. In addition, we followed this quasar up with the TripleSpec spectrograph (Wilson et al. 2004) on the Hale 200-inch telescope (P200) at the Palomar Observatory on 2013 Feb 24. Four exposures of 200 seconds are taken in an A-B-B-A dithering mode. The 1-D spectrum is then retrieved using the IDL SpexTool package (Cushing et al. 2004). With a higher spectral resolution and a broader wavelength coverage, the TripleSpec data thus render higher precision in measuring absorption lines and emission lines than the archival VLT/ISAAC spectrum of F11119+3257. All photometric and spectroscopic data are corrected for Galactic extinction at  $E_{B-V} = 0.02$  according to the updated dust map of Schlafly & Finkbeiner et al. (2011). Before follow-up analysis, all data are deredshifted at  $z = 0.18966 \pm 0.00006$  determined using the narrow emission lines (§3.2.2), and the laboratory vacuum wavelengths of the lines studied in this paper are adopted from Vanden Berk et al. (2001) (optical), Landt et al. (2008) (NIR), Sturm et al. (2002) (mid-IR [MIR]), and corresponding references therein.

## 3. DATA ANALYSIS

### 3.1. Spectral Energy Distribution and Extinction

Inspecting the broad-band SED of F11119+3257 from optical to Mid-infrared, we find its color to be exceedingly red ( $(u-W_1)_{\text{F11119+3257}} \sim 11.3$ ) as compared to typical type-1 quasars (i.e.  $(u-W_1)_{3C\ 273} \sim 4.3$ ) or even typical ULIRGs ( $(u-W_1)_{\text{Mrk 231}} \sim 7.8$ ). Therefore, heavy extinction in the optical band is expected in F11119+3257. Balmer emission line ratio of F11119+3257 also indicates an extinction to the Broad Emission-Line Region (BELR) at  $E_{B-V} \approx 1.08$  (Zheng et al. 2002). F11119+3257 is therefore heavily reddened, and its extinction curve needs to be figured out before modeling of the spectrum.

---

<sup>1</sup><http://nesssi.cacr.caltech.edu/DataRelease/>

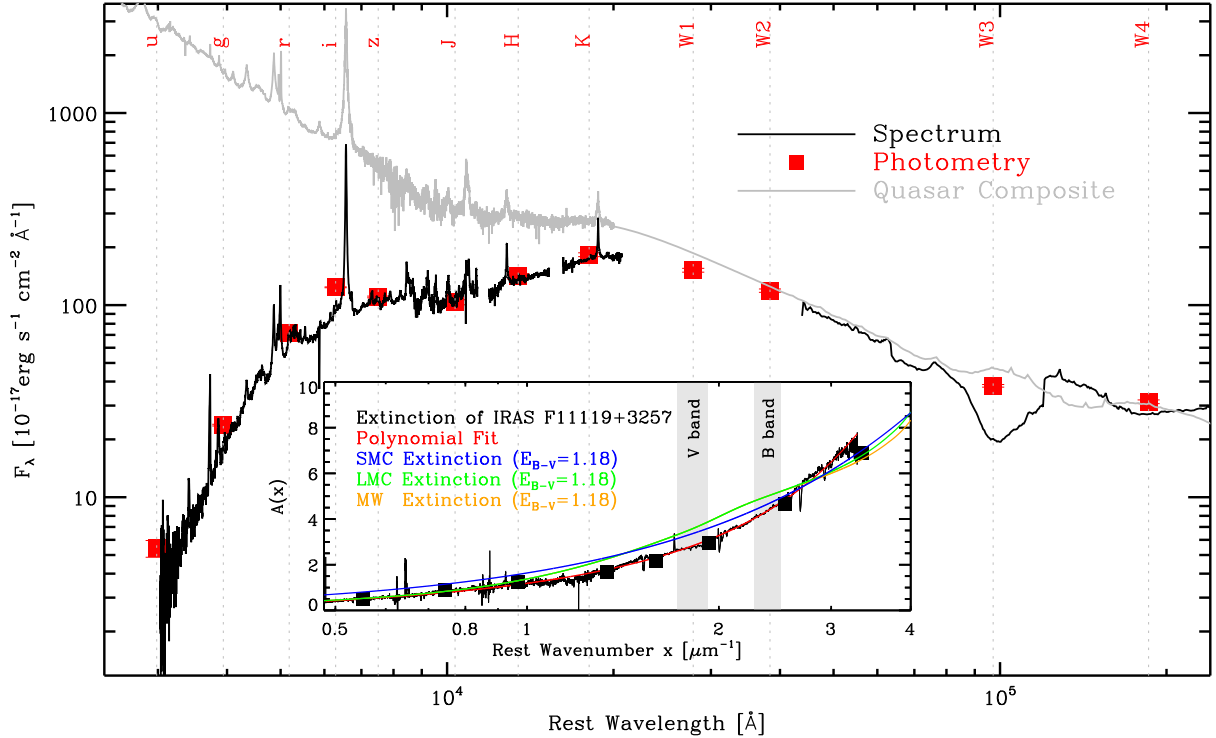


Fig. 1.— SED and Extinction curve (inner panel) of F11119+3257. The spectrum (black lines) and photometric data (red squares) are compared with the quasar composite scaled at *WISE*  $W_4$  (grey solid line). The observed extinction curve of F11119+3257 (black line in the inner pannel) is compared with SMC (blue), average LMC (green) and average MW (orange) extinction curves at a similar color excess of  $E_{B-V} = 1.18$ .

Since stellar absorption features are not obviously seen in F11119+3257, starlight can be ignored. And scattered AGN radiation, which usually results in a blue continuum in obscured quasars (Li et al. 2015), is also negligible as the flux density at the blue end of the spectrum is low. It is thus assumed that the optical-IR continuum of F11119+3257 is dominated by the obscured AGN emission. By comparing the SED of F11119+3257 with the quasar composite (Zhang et al. 2017, a combination of the optical, NIR, and FIR quasar composite from Vanden Berk et al. 2001, Glikman et al. 2006, and Netzer et al. 2007 respectively), we find they agree roughly with each other in the MIR ( $\sim \lambda \in [3, 30]\mu\text{m}$ , see Figure 1). And significant extinction can be seen in both the optical band and the NIR, therefore the physical extent of the obscurer should be large enough to fully cover both disk continuum and hot/warm blackbody radiation from the torus. Since the optical-IR SED of F11119+3257 is dominated by the transmitted AGN radiation, we follow the conventional method of assuming the quasar composite as the extinction-free spectrum in deriving the extinction curve. After scaling the quasar composite to F11119+3257 at *WISE*  $W_4$ , its extinction curve is then calculated,  $A_\lambda = -2.5 \times \log(F_\lambda^{\text{F11119+3257}}/F_\lambda^{\text{composite}})$  (inner panel of Figure 1). This extinction curve is then fitted with a cubic polynomial, which is  $A(x) = -0.22 + 1.22x + 0.12x^2 + 0.07x^3$ , where  $x = (\lambda/1\mu\text{m})^{-1}$ . Consisting of only 4 polynomial coefficients, the model of extinction curve is so simple that the effect of high-frequency spectral noises, i.e. sharp dips and peaks around emission and absorption lines, is largely avoided. After applying the response curve of *B*, *V* filter (Johnson & Morgan 1953), broad-band extinction and color

excess of F11119+3257 are calculated:  $A_V = 2.78$ ,  $E_{B-V} = 1.18$ . The extinction value is similar to that estimated for the BELR of  $E_{B-V} \approx 1.08$  (Zheng et al. 2002). Studying of the First-2MASS red quasars shows that the  $E_{B-V}$  estimated for emission-line regions are relatively more uncertain as compared to the  $E_{B-V}$  estimated for AGN continuum (Glikman et al. 2007). The reason is that properties of quasar BELs are diverse and could deviate from Case-B recombination in certain objects. On the other hand, Dong et al. (2008) found that the broad-line  $H\alpha/H\beta$  line ratio of blue AGNs peaks at 3.06 (with a relatively small spread of 0.22), suggesting that Balmer decrement can indicate  $E_{B-V}$  in normal AGNs. Thus the remarkable agreement between the extinction evaluated for both the continuum and the BELR indicates that F11119+3257 follows general properties of AGNs and the extinction evaluations are reasonable. In comparison with extinction curves of SMC, average LMC, and average Milky Way at  $E_{B-V} = 1.18$  (Prevot et al. 1984; Fitzpatrick 1986; Fitzpatrick & Massa 2007), we find that the extinction curve of F11119+3257 is relatively steeper. Such kind of steep extinction curve is similar to those reported in many other BAL quasars (e.g. Jiang et al. 2013; Zafar et al. 2015).

### 3.2. Emission Lines

#### 3.2.1. Continuum and Fe II Multiplets

Before modeling Emission Lines, broad spectral features, i.e. the continuum and the Fe II multiplets, needs to be subtracted. For the featureless continuum, we first select multiple continuum regions with widths of  $\Delta\lambda/\lambda = 0.001$  (triangles in the top panel of Figure 2). We then interpolate these continuum points into the entire spectrum in  $\log \lambda$ - $\log F_\lambda$  space (dashed lines in Figure 2.1) and obtain the baseline model of the underlying continuum.

The baseline underlying continuum is then subtracted, and the Fe II multiplets are fitted in the four spectral regions showing prominent Fe II emissions. They are  $[4400,4700]\text{\AA}$ ,  $[5120,5700]\text{\AA}$ ,  $[6000,6270]\text{\AA}$  and  $[6950,7350]\text{\AA}$  in quasar’s rest frame (grey shaded regions in Figure 2.1). Following Dong et al. (2011), a two-component analytic form of Fe II emission lines incorporating the VJV04 Fe II template (Véron-Cetty et al. 2004) are used as the model. The narrow one of the two Fe II components is assigned with a Gaussian profile. Both Gaussian and Lorentzian profiles are tested for the broad Fe II component. Similar to many other NLS1s, the Lorentzian profile approximates the data better. On the other hand, though, it is found that this Fe II model cannot fit the data well, as the Fe II flux ratio in the Fe II windows of F11119+3257 is quite different to that of the VJV04 template: after the removal of the interpolated continuum, the integrated Fe II flux ratio of F11119+3257 at the  $\lambda_{4570}$  ( $[4400,4700]\text{\AA}$ ) and the  $\lambda_{5250}$  ( $[5120,5700]\text{\AA}$ ) windows is  $F_{4570}/F_{5250} = 0.35$ , much lower than that of the template quasar I Zw 1,  $F_{4570}/F_{5250}(\text{IZw1}) = 0.92$ . The relatively low flux of Fe II emission at shorter wavelengths in F11119+3257 indicates significant reddening of the Fe II emission. We thus apply the cubic polynomial extinction curve of F11119+3257’s continuum (§3.1) to the Fe II multiplets, with a scaling factor variable  $E_{B-V}^{\text{Fe II}}$ . Even though continuum windows are selected to avoid Fe II lines, some continuum points can still be contaminated by Fe II emissions. In order to solve the entanglement between continuum and Fe II multiplets, we performed the modeling iteratively:

Step 1, interpolate continuum points (orange triangles in Figure 2.1) to the spectrum in  $\log \lambda$ - $\log F_\lambda$  space to obtain continuum model (orange dashed lines in Figure 2.1).

Step 2, subtract the continuum model and fit the Fe II emission in the four Fe II windows (orange solid line in Figure 2.1).

Step 3, subtract the Fe II emission model at continuum points and obtain the corrected continuum fluxes

(red triangles in Figure 2.1).

Step 4, repeat Step 1-3 until the fitted Fe II fluxes converge (with a precision of 1%).

Finally, at a best-fit of  $\chi^2/\text{DOF} \sim 1.1$ , modeled continuum and Fe II emissions are obtained (red lines in Figure 2.2). The best-fit profile parameters of the Fe II emission lines are listed in Table 2, and extinction to the Fe II emission is calculated to be  $E_{B-V}^{\text{Fe II}} = 1.4 \pm 0.1$ . The uncertainty of continuum+Fe II multiplets is shown with pink shaded areas in the lower three panels of Figure 2, which is derived with a bootstrap approach. The continuum+Fe II multiplets model is then subtracted before follow-up analysis of the emission lines.

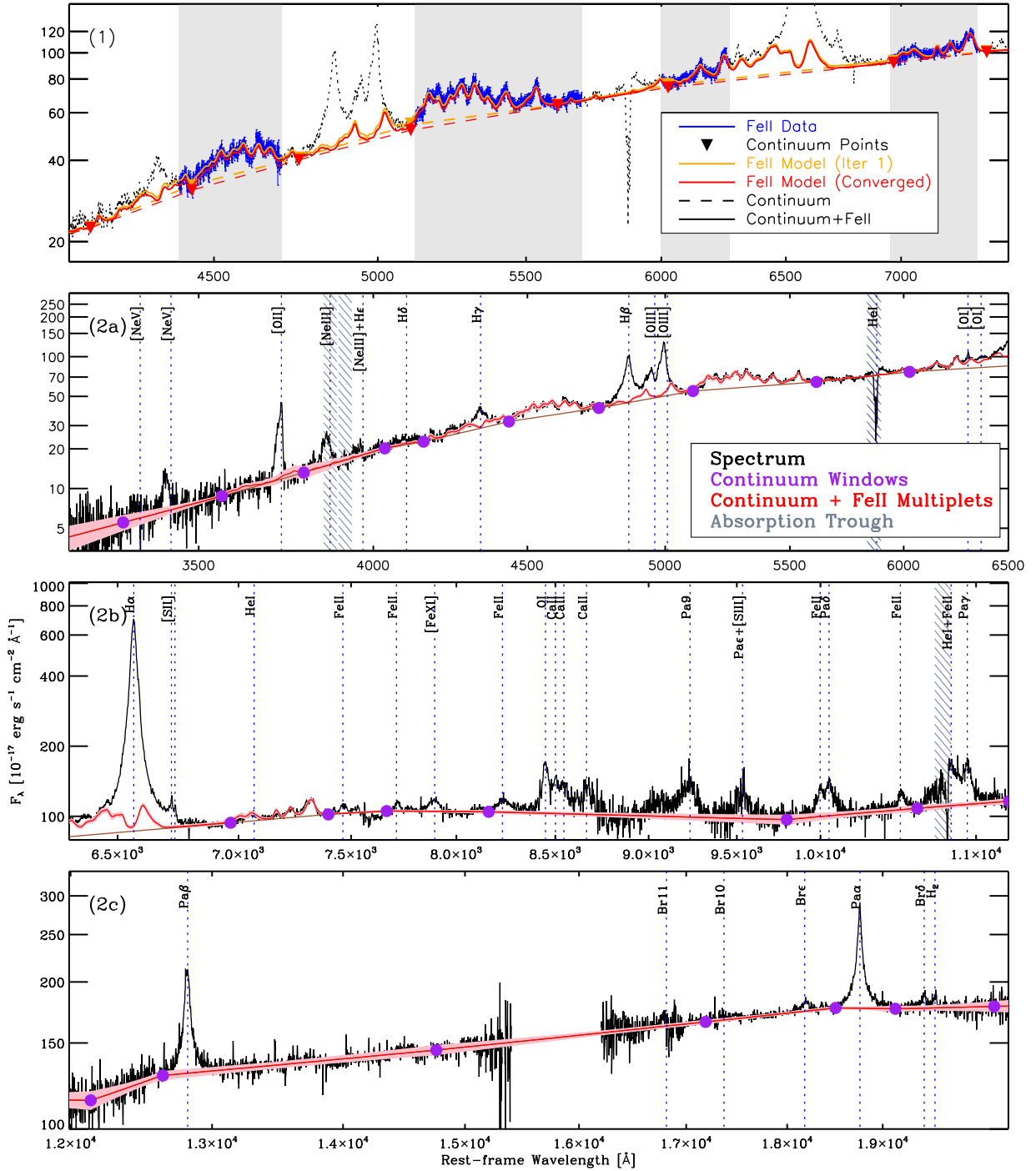


Fig. 2.— Modeling of the continuum and the Fe II multiplets are shown in panel (1). Data points in the four Fe II windows are colored blue. The results w/o been modeled iteratively are colored red and orange respectively (see §3.2.1 for a detailed description). Modeled continuum and continuum+Fe II are presented with dashed and solid lines. In panel (2a), (2b), (2c), the modeled continuum points are indicated with purple dots. The best-fit and the uncertainty of continuum + Fe II multiplets model are shown with red lines and pink shades. We mark laboratory wavelengths of common emission lines with vertical lines. Spectral regions shaded by tilted lines indicate spectral regions affected by Broad Absorption Lines (BALs, §3.3). The marked BALs are He I\*  $\lambda$ 3889, Ca II  $\lambda$ 3934, Na I  $\lambda\lambda$ 5891,5897 in panel (2a), and He I\*  $\lambda$ 10830 in panel (2b).

### 3.2.2. Broad Emission Lines and Narrow Emission Lines

In the bottom three panels of Figure 2, an overview of F11119+3257’s emission lines is shown. We mark the laboratory wavelengths of the emission lines at a rest frame of  $z = 0.18966 \pm 0.00006$  (see detailed description below) with dotted vertical lines.

At the first glance, the peak of strong Balmer, Paschen, and Brackett emission lines matches the dotted vertical lines. Also, the peaks of low-ionization forbidden lines like [O II]  $\lambda$  3727 and [S II]  $\lambda\lambda$ 6718,6732 match their dotted line marks, indicating that they share a similar systemic redshift. Since no obvious stellar absorption is detected, low-ionization Narrow Emission Lines (NELs) appear to be the best redshift indicator of F11119+3257. [O II]  $\lambda$  3727 emission line is commonly used as a redshift indicator. However, this doublet in F11119+3257 is highly asymmetric (Figure 5.4), indicating that significant portion of it is contributed by non-NEL components. Thus the systemic redshift of the quasar cannot be measured directly with the [O II]  $\lambda$  3727 emission line. Other optical low-ionization forbidden emission lines, i.e. O I  $\lambda$  6302, [N II]  $\lambda\lambda$ 6549,6585 and [S II]  $\lambda\lambda$ 6718,6732 are blended with the prominent H $\alpha$  emission line. We thus have to model these narrow emission lines together with H $\alpha$  in the observed wavelength range of [7471,8090]Å ([6280,6800]Å at  $z = 0.18966$ ). During the modeling, all these narrow emission lines are assumed to be Gaussians with the same *FWHM*, and their central wavelengths ratios are fixed as their laboratory wavelengths ratios. The flux ratio of the [N II] doublet is fixed at  $F_{[\text{N II}] \lambda 6549}/F_{[\text{N II}] \lambda 6585} = 1/2.96$ . On the other hand, five Gaussians (one narrow component at  $FWHM < 1000\text{km s}^{-1}$  and four broad components at  $FWHM > 1000\text{km s}^{-1}$ ) are assumed for H $\alpha$  to ensure a reasonable fit and a reliable determination of the relatively weak NELs. Redshift of the NEL system is found to be  $z = 0.18966 \pm 0.00006$ , which is regarded as the systemic redshift of F11119+3257. The modeled Gaussian width is  $FWHM = 570 \pm 40\text{km s}^{-1}$  (Table 2). Fitting results are shown in panel (1a) of Figure 3. And modeled weak NELs are presented together with the Fe II multiplets model and the residual in panel (1b).

As shown in Figure 2, the most prominent broad Hydrogen emission lines are Pa $\alpha$ , Pa $\beta$ , H $\alpha$ , and H $\beta$ . Among them, H $\alpha$  is blended with several weak NELs, and H $\beta$  is blended with the blueshift [O III]  $\lambda\lambda$  4959,5007 emission lines. After removal of the modeled NELs, line profile of H $\alpha$  is obtained. Line spectrum around H $\beta$  and [O III] is shown in panel (2a) of Figure 3. And the removed Fe II multiplets model is presented in panel (2b). The subtraction of the Fe II multiplets seems reasonable and the line profiles of H $\beta$  and [O III] can be reliably obtained. For the H $\beta$  + [O III] blend, we begin with solving the line profile of the [O III] doublet. After scaling the H $\alpha$  profile to match the peak of H $\beta$  emission (panel 2a of Figure 3), we found that in the rest-frame wavelength range of [4940,5020] (grey shaded region), the contribution of H $\beta$  emission is negligible (weaker than the spectral flux fluctuations). Therefore, the emission of [O III]  $\lambda\lambda$  4959,5007 should dominate in this spectral region. In addition, the bulk flux of [O III]  $\lambda$  5007 lies in this spectral region, as well as the peak of [O III]  $\lambda$  4959. By convention, the line profile of [O III]  $\lambda$  4959 and [O III]  $\lambda$  5007 are assumed to be the same and the line ratio are fixed at  $F_{[\text{O III}] \lambda 4959}/F_{[\text{O III}] \lambda 5007}=1/2.98$  (Storey & Zeippen 2000). We then solve the line spectrum in this region pixel by pixel, and obtain the emission line profile of [O III]  $\lambda$  5007 and [O III]  $\lambda$  4959 (blue and green solid line in panel 2a of Figure 3). Finally, after the subtraction of [O III]  $\lambda\lambda$  4959,5007, the line profile of H $\beta$  is derived.

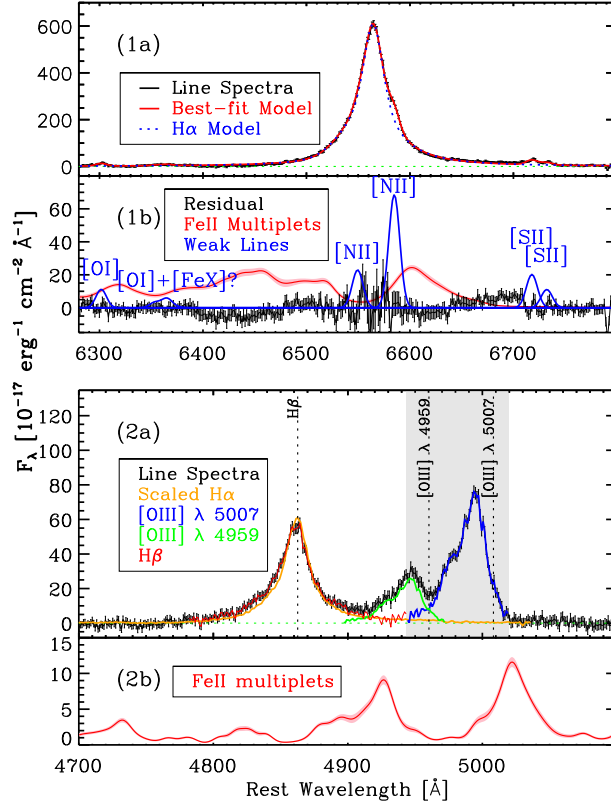


Fig. 3.— Modeling of the H $\alpha$  blend is shown in panel (1a). Although the modeled NELs are weak, they can still be distinguished from FeII multiplets and model residuals as shown in pane (1b). The H $\beta$  and [OIII] blend is shown in panel (2a). The profile of [OIII]  $\lambda$  5007 (blue solid line) is derived in the grey shaded region, where FeII emission (panel 2b) is reliably removed and contribution from H $\beta$  is negligible. The derived [OIII]  $\lambda\lambda$  4959,5007 emission is subtracted and the H $\beta$  emission line (red solid line in panel 2a) is obtained.

The flux-weighted centroid velocities and  $FWHM$ s of these four Hydrogen emission lines are measured and shown in Table 2, which differ significantly from each other. As the wavelength decreases from Pa $\alpha$  through Pa $\beta$  and H $\alpha$  to H $\beta$ , the line centroids vary gradually from at  $\sim 0$  km s $^{-1}$  to be blueshifted at  $\sim 100$  km s $^{-1}$  in quasars rest frame. And the  $FWHM$  increases gradually from  $\sim 900$  km s $^{-1}$  to  $\sim 1450$  km s $^{-1}$ . Such a trend of their profile changing suggests that these Hydrogen emission lines are not dominated by a same single component. Being permitted lines of the most abundant element in the universe, Hydrogen Balmer/Pashen emissions can be generated in various astrophysical environments. Thus, the emission line systems in F11119+3257: the Narrow Emission Lines, the Broad Emission Lines (BELs), and the blueshifted Outflow Emission Line (OEL, §3.2.3) systems may all contribute to these observed Hydrogen emission. And different intensity ratios of these emission-line systems can lead to the line-profile variations observed among these Hydrogen lines. A brief comparison among the Hydrogen lines is then made as an attempt to investigate the emission-line components.

Despite their differences, the red wings of these Hydrogen lines resemble each other (in a velocity range

of  $[200,4000]\text{km s}^{-1}$  in quasar’s restframe). This is reasonable since the line flux in this velocity region is dominated by only the BEL system, which leads to the similarity of line profiles in this region. In Figure 4, different Hydrogen lines are scaled by their fluxes in their red wings (in a velocity range of  $[200,4000]\text{km s}^{-1}$ ), and their profiles are compared. The  $\text{Pa}\alpha$  emission line has the largest wavelength and thus lowest extinction, i.e. least affected by obscuring dust. We therefore use the line profile of  $\text{Pa}\alpha$  as a reference since it preserves best the BEL component among these Hydrogen lines. The line profile of  $\text{Pa}\alpha$  and  $\text{Pa}\beta$  are similar in both their blue and red wings, while a narrow peak is found in only  $\text{Pa}\alpha$  and none of the other Hydrogen lines. The difference between  $\text{Pa}\alpha$  and Balmer lines lies in two aspects (Figure 4.2, 4.3, 4.4). 1) The sharp and narrow peak of  $\text{Pa}\alpha$  appears prominent if  $\text{Pa}\alpha$  is compared with Balmer lines. 2) Significant residual fluxes are found in the blue wings of Balmer lines if scaled  $\text{Pa}\alpha$  profile is subtracted. Using  $\text{Pa}\alpha$  as a baseline model for the broad and narrow Hydrogen emission line component, the residual fluxes in the blue wings of Balmer lines are very likely associated with the other blueshifted emission lines like  $[\text{O III}]$ ,  $[\text{Ne III}]$ , and  $[\text{Ne V}]$ . Since the Balmer BELs are suppressed more severely by dust extinction than the Paschen BELs, the relatively weak blueshifted Emission line components can be revealed in the blue wings of the Balmer lines. If this is the case, the OEL component then should be more easily observed in lines whose BEL endures stronger extinction, i.e. at shorter wavelengths, as in the case of the obscured quasar OI 287 (Li et al. 2015). This phenomenon is indeed observed, the relatively strength of residual flux in blue wings of  $\text{H}\beta$  is noticeably stronger than  $\text{H}\alpha$ . And for  $\text{H}\gamma$  at a even shorter wavelength, the residual in the blue wing can be clearly seen under low signal-to-noise ratio even if the potential  $[\text{O III}] \lambda 4363$  emission is treated as part of  $\text{H}\gamma$  emission in the red wing. Since this residual flux is most clearly observed in  $\text{H}\beta$ , this blueshifted component is retrieved by subtracting the scaled  $\text{Pa}\alpha$  line profile, and will be investigated later in the follow-up section.

On the other hand, we find that the centers of all Hydrogen emission lines are flat except that a weak but prominent narrow emission is found in the peak of  $\text{Pa}\alpha$ . By subtracting the profile of  $\text{H}\alpha$  (the Hydrogen line with the highest signal-to-noise ratio), the narrow  $\text{Pa}\alpha$  peak is detected (brown line in Figure 4.2) at a flux of  $F_{\text{Pa}\alpha \text{ peak}} = 370 \pm 90 \times 10^{-17} \text{ergs}^{-1} \text{cm}^{-2}$ . And the width of the peculiar narrow emission component is ( $FWHM_{\text{Pa}\alpha \text{ peak}} = 260 \pm 20 \text{ km s}^{-1}$ ), significantly lower than the NEL component ( $FWHM_{\text{NEL}} = 570 \pm 40 \text{ km s}^{-1}$ ). We then check this narrow Paschen emission in  $\text{Pa}\beta$ . By subtracting the scaled  $\text{H}\alpha$  from  $\text{Pa}\beta$ , the excess flux at the peak of  $\text{Pa}\beta$  is found to be  $F_{\text{Pa}\beta \text{ peak}} = 40 \pm 60 \times 10^{-17} \text{ergs}^{-1} \text{cm}^{-2}$ , consistent with non-detection. Therefore, the line ratio  $\text{Pa}\beta / \text{Pa}\alpha$  for this narrow emission is quite low ( $F_{\text{Pa}\beta \text{ peak}} / F_{\text{Pa}\alpha \text{ peak}} < 0.15$ ) if case-B flux ratios of ( $F_{\text{Pa}\alpha} / F_{\text{Pa}\beta} \approx 0.5$ ) is considered (Hummer & Storey 1987). Positively detected only in  $\text{Pa}\alpha$ , this anomalous narrow Paschen emission is thus much weaker at shorter wavelength as compared to model predictions. The most plausible explanation to this phenomenon is that this Paschen emission-line component is heavily reddened. By assuming an extinction law of either MW (Fitzpatrick & Massa 2007) or SMC (Prevot et al.1984), an  $H$  band ( $\lambda_{\text{eff}} \approx 16620 \text{ \AA}$ ) extinction of  $A_H > 2.1$  (corresponding to  $E_{B-V} > 3.7$ ) can be figured. The low velocity dispersion and high extinction makes this emission line component distinct from all the other emission line systems verified in the quasar F11119+3257, and it will be discussed later in §4.3.

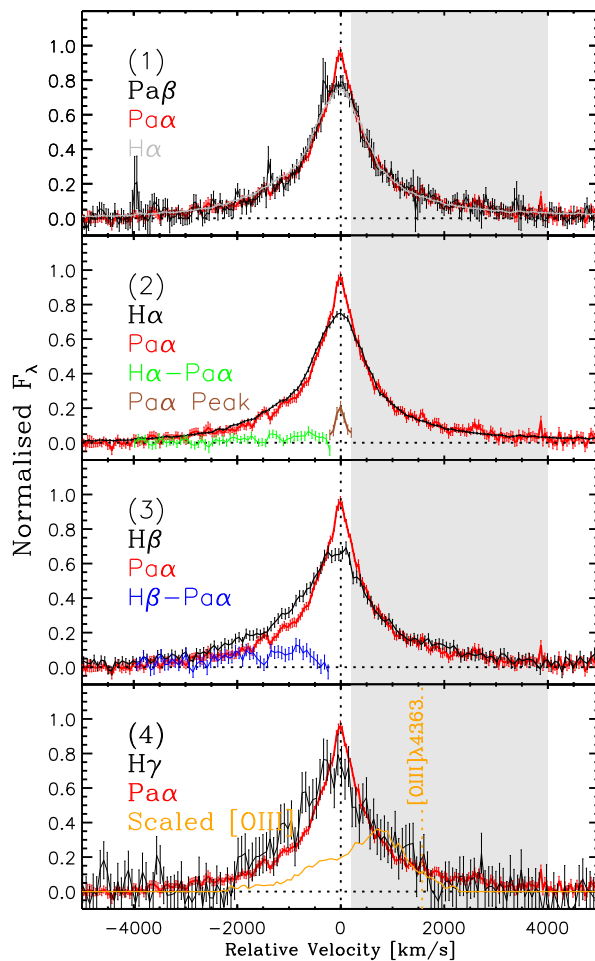


Fig. 4.— From top to bottom panels, emission line profiles of  $\text{Pa}\beta$ ,  $\text{H}\alpha$ ,  $\text{H}\beta$ , and  $\text{H}\gamma$  are compared with that of  $\text{Pa}\alpha$ . All emission lines are normalized by their integrated flux in the grey shaded region ( $[200,4000]\text{km s}^{-1}$  in velocity space). A sharp narrow peak unique in  $\text{Pa}\alpha$  is found (brown lines), and significant residual fluxes in the blue wings of  $\text{H}\alpha$  (green lines),  $\text{H}\beta$  (blue lines), and  $\text{H}\gamma$  are detected.

### 3.2.3. Outflow Emission Lines

As shown in the lower panels of Figure 2, the high-ionization forbidden lines like  $[\text{O III}] \lambda\lambda 4959, 5007$  and  $[\text{Ne V}] \lambda 3427$  are all significantly blueshifted in the rest frame of the quasar. Significant flux excess in the blue wings are also detected in  $[\text{O II}] \lambda 3727$ ,  $[\text{Ne III}] \lambda 3869$ , and  $[\text{Ne III}] \lambda 3968$ . On the other hand, blueshifted residual fluxes in  $\text{H}\alpha$  and  $\text{H}\beta$  (§3.2.2) are found. They can all originate from the outflow gas.

The blueshifted emission lines,  $[\text{O III}] \lambda 5007$ ,  $[\text{O II}] \lambda 3727$ ,  $[\text{Ne III}] \lambda 3869$ ,  $[\text{Ne III}] \lambda 3968$ ,  $[\text{Ne V}] \lambda 3427$ , as well as the residual  $\text{H}\alpha$  and  $\text{H}\beta$  emission are plotted together in the Figure 5. It is found that for all these lines, the majority of blueshifted emission are in a similar velocity range of  $\sim[-3500, 0] \text{ km s}^{-1}$ . For  $[\text{O III}]$

$\lambda 5007$ ,  $[\text{O II}] \lambda 3727$ , and  $[\text{Ne III}] \lambda 3869$ , significant amount of flux at  $v=0 \text{ km s}^{-1}$  are detected, which can come from the NEL fluxes centered at  $v = 0 \text{ km s}^{-1}$  (§3.2.2). This should be removed before analyzing the blueshifted emission line system. We assume that the NEL component of  $[\text{O III}] \lambda 5007$  and  $[\text{O II}] \lambda 3727$  to be symmetric about  $v=0 \text{ km s}^{-1}$ , and the flux at  $v > 0 \text{ km s}^{-1}$  are dominated by the NEL component. The “NEL” component (green dashed line in Figure 4) of  $[\text{O III}] \lambda 5007$  and  $[\text{O II}] \lambda 3727$  are then obtained and subtracted, which leaves the blueshifted emission line components (blue dashed lines in Figure 5).

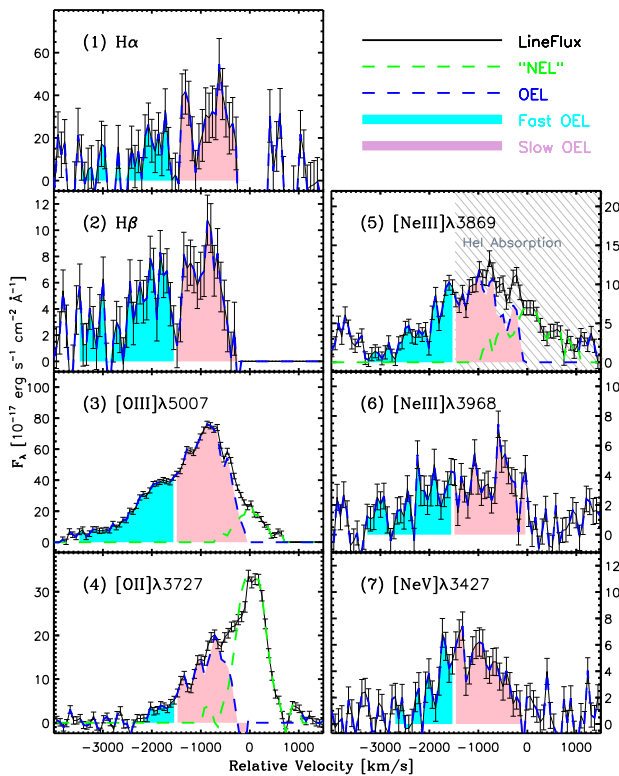


Fig. 5.— Blueshifted emission lines in F11119+3257, i.e. (1) residual  $\text{H}\alpha$ , (2) residual  $\text{H}\beta$ , (3)  $[\text{O III}] \lambda 5007$ , (4)  $[\text{O II}] \lambda 3727$ , (5)  $[\text{Ne III}] \lambda 3869$ , (6)  $[\text{Ne III}] \lambda 3968$ , (7)  $[\text{Ne V}] \lambda 3427$  are shown in the figure. The symmetric “NEL” system centered at  $v = 0 \text{ km s}^{-1}$  is presented with green dashed line. The fast and slow OEL components are shaded cyan and pink respectively, and their total fluxes are marked with blue dashed lines. The slow OEL component of  $[\text{Ne III}] \lambda 3869$  can be affected by  $\text{He I}^* \lambda 3889$  mini-BAL (shaded with grey lines).

This blueshifted emission line system, or the so-called  $[\text{O III}]$  “blue outliers”, are usually referred to as tracers of outflows (Komossa et al. 2008). We thus call them Outflow Emission Lines (OELs) in the follow-up analysis. This OEL system is broad ( $FWHM_{[\text{O III}] \lambda 5007} = 1514 \text{ km s}^{-1}$ ). In  $[\text{O III}] \lambda 5007$ , the OEL with the highest spectral quality, a peak at  $v \sim -800 \text{ km s}^{-1}$  is found. In addition to this low-speed peak, another broad component can be found that is centered at around  $v \sim -2000 \text{ km s}^{-1}$ . It seems that the  $\text{H}\beta$  and  $[\text{Ne III}]$  OEL also follow such a two-component scenario. We thus divide the OEL system into a high-speed component (fast OEL;  $v \in [-3500, -1500] \text{ km s}^{-1}$ ) and a low-speed component (slow OEL;  $v \in (-1500, 0]$ ).

km s<sup>-1</sup>). The integrated fluxes of both the fast OEL and the slow OEL components, and flux-weighted average velocities for each lines are listed in Table 3. Notice that the slow OEL component of [Ne III]  $\lambda$ 3869 can be contaminated by the He I\*  $\lambda$  3889 mini-BAL (marked region in panel 5 of Figure 5), the integrated flux in this region is therefore a lower limit estimation.

### 3.3. Broad Absorption Lines and Column Densities

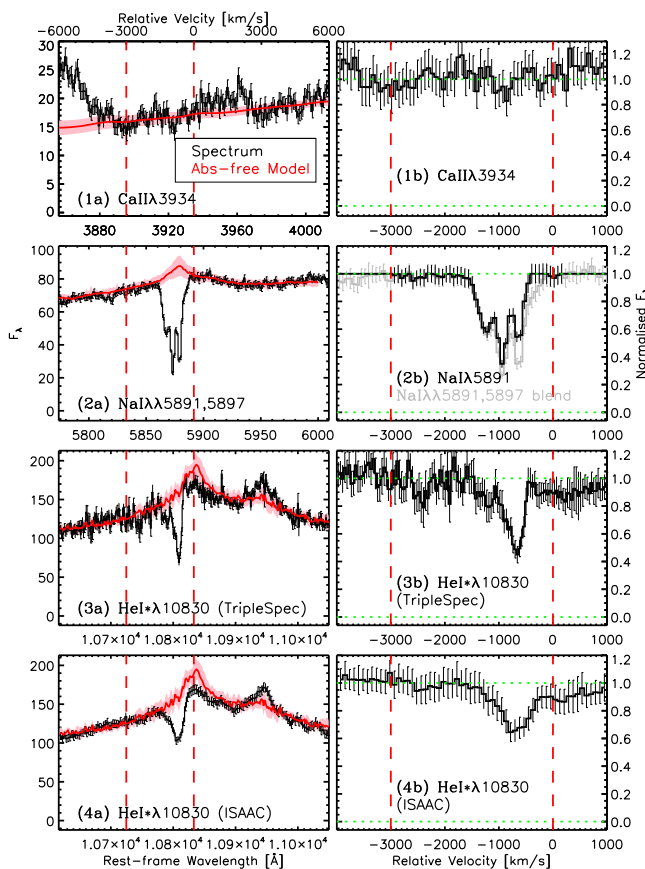


Fig. 6.— Spectrum of F11119+3257 around the Ca II  $\lambda$  3943, Na I  $\lambda\lambda$  5891,5897 and He I\*  $\lambda$  10830 mini-BALs as well as absorption-free models (red lines) and model uncertainties (pink shades) are shown in the left panels. Normalized spectrum are shown in the right panels. By integrating AOD in a velocity range of  $[-3000,0]$  km s<sup>-1</sup> (red vertical dashed lines), column densities are derived:  $\log N_{\text{Ca}^+}/\text{cm}^{-2} < 14.0$   $\log N_{\text{Na}^0}/\text{cm}^{-2} = 13.7 \pm 0.1$  and  $\log N_{\text{He}^0(2^3\text{S})}/\text{cm}^{-2} > 13.2$ .

Besides the Na I  $\lambda\lambda$  5891,5897 mini-BAL (Rupke et al. 2005) and the blueshifted molecular OH absorption line (Veilleux et al. 2013), we noticed prominent metastable He I\*  $\lambda$  10830 and weak Ca II  $\lambda$ 3934 absorption lines in the optic-NIR spectrum of F11119+3257. The absorption troughs lie in a velocity range of  $v \sim [-3000,0]$  km s<sup>-1</sup> (centered at  $\sim -1000$  km s<sup>-1</sup>) relative to the systemic redshift of  $z = 0.18966$ ,

very similar to the OELs (Table-3). As presented in §3.1, the optical-NIR spectrum of F11119+3257 is dominated by the transmitted AGN radiation. The dust absorber appears to fully cover the AGN radiation in our sightline (covering factor is about 1), since both the reflected AGN emission and the starlight from host galaxy are negligible.

For the weak absorption of Ca II  $\lambda$  3934, no prominent emission lines are found around the absorption trough. The continuum + Fe II model described in §3.2.1 is a reasonable normalization in this spectral region (Figure 6.1a). Based on the normalized Ca II  $\lambda$  3934 absorption profile (Figure 6.1b), we integrate the apparent optical depth (AOD, Savage & Sembach 1991) in the velocity range of  $v \in [-3000, 0]$  km s<sup>-1</sup> and derive the upper limit of the ion Ca<sup>+</sup>'s column density to be  $\log N_{\text{Ca}^+}/\text{cm}^{-2} < 14.0$ . On the other hand, the Na I  $\lambda\lambda$ 5891,5897 blend and the He I\*  $\lambda$ 10830 absorption are close to emission lines (He I  $\lambda$ 5877 and He I\*  $\lambda$ 10830 + Pa $\gamma$  respectively), which makes simple continuum model invalid in approximating the absorption-free spectrum. Following Liu et al. (2015), we apply pair-matching method to normalize these two absorption lines. For the Na I  $\lambda\lambda$ 5891,5897 blend, spectra of SDSS DR12 quasars (Pâris et al.2017) at  $z < 0.5$  are used as templates. Similar to Liu et al.(2016), we fix an optical depth ratio of  $\tau_{\text{NaI } \lambda 5891}/\tau_{\text{NaI } \lambda 5897} = 2$  and obtain the absorption line profile of Na I  $\lambda$ 5891 (black line in Figure 6.2b). By integrating AOD, the column density of atomic sodium is found to be  $\log N_{\text{Na}^0}/\text{cm}^{-2} = 13.7 \pm 0.1$ . Pair-matching method is then performed to normalize the He I\*  $\lambda$ 10830 min-BAL, with 92 infrared quasar spectra from infrared quasar spectral atlases (Glikman et al. 2006, Riffel et al. 2006, Landt et al. 2008). We assume a covering factor of 1 and measure the column density of atomic helium in the metastable 2<sup>3</sup>S state via calculating AOD. The results based on the P200/Triplespec and the VLT/ISAAC data are  $\log N_{\text{He}^0(2^3\text{S})}/\text{cm}^{-2}(\text{TripleSpec}) = 13.4 \pm 0.2$  and  $\log N_{\text{He}^0(2^3\text{S})}/\text{cm}^{-2}(\text{ISAAC}) = 13.3 \pm 0.3$ , consistent with each other. Provided that the Triplespec data has higher resolution and shows more detailed absorption features, we adopt the more reliable Triplespec result in the follow-up analysis. Since emission line spectrum around He I\*  $\lambda$ 10830 is complex, and the number of template spectra is limited, the normalization is not as good. In addition to the He I\*  $\lambda$  10830 + Pa $\gamma$  BEL, there can be significant He I\*  $\lambda$ 10830 OEL (in the velocity range of  $v \in [-3500, 0]$  km s<sup>-1</sup>described in §3.2.3) in the absorption trough. In the meantime, part of the IR radiation comes from blackbody components (§3.1), which may not be fully covered by the absorbing gas. In view of these facts, the directly normalized He I\*  $\lambda$ 10830 absorption can be significantly underestimated, it is thus regarded as the lower limit of the column density for the metastable atomic helium, i.e.  $\log N_{\text{He}^0(2^3\text{S})}/\text{cm}^{-2} > 13.2$ . In view of the uncertainty in measuring He I\*  $\lambda$ 10830 absorption, the corresponding He I\*  $\lambda$ 3889 absorption remains unknown. The potential He I\*  $\lambda$ 3889 absorption trough lies just beneath the [Ne III]  $\lambda$  3869 slow OEL component. Thus the integrated flux of [Ne III]  $\lambda$  3869 slow OEL can only be treated as a lower-limit estimate (Figure 5.5).

### 3.4. FIR Continuum and Emission Lines

The Spitzer IRS spectrum of F11119+3257 obtained from ‘‘Cornell Atlas of Spitzer/IRS Sources’’ (CASIS LR7; Lebouteiller et al. 2011) is shown in Figure 7. Significant silicate absorption at  $\sim 9.7 \mu\text{m}$  is found, as well as several conspicuous PAH emission features. We modeled the Spitzer spectrum of F11119+3257 with PAHFIT (v1.2). PAHFIT is an IDL tool that decomposes Mid-Infrared spectrum into reddened starlight, thermal dust continuum, and various emission lines. More detailed setup of the modeling can be found in Smith et al. (2007). Based on the best-fit result of PAHFIT, the combined luminosity of PAH 6.2  $\mu\text{m}$  and PAH 11.2  $\mu\text{m}$  is  $L_{\text{PAH}(6.2\mu\text{m}+11.2\mu\text{m})} = 5.0 \pm 0.6 \times 10^{43}$  erg s<sup>-1</sup>. Applying the relation of  $SFR(M_{\odot}, \text{yr}^{-1}) = 1.18 \times 10^{41} L_{\text{PAH}(6.2\mu\text{m}+11.2\mu\text{m})}$  (typical error is of the order 50%; Farrah et al. 2007), the star formation rate ( $SFR$ ) of F11119+3257 is estimated to be  $SFR_{\text{PAH}} = 600 \pm 300 M_{\odot} \text{yr}^{-1}$ . Harboring a lu-

minous AGN, the ionizing photons from the nucleus can affect the presence and emission line strengths of PAH particles in F11119+3257. Thus the star formation rate cannot be precisely quantified by measuring PAH emissions. Since the FIR luminosity of F11119+3257 can be derived, we can also evaluate SFR based on the correlations of these two quantities. By checking the IRAS and the SCUBA photometries of F11119+3257 (Table-1), we obtain the FIR luminosity (30-850 $\mu\text{m}$ ) of cold dust emission in F11119+3257  $L_{\text{FIR}} = 2.1 \pm 0.3 \times 10^{46} \text{erg s}^{-1}$ . The contribution of the star-burst activity to the FIR luminosity is estimated to be  $\sim 20\%$  based on the restframe  $f_{15}/f_{30}$  ratio (ratio between continuum fluxes at 15 $\mu\text{m}$  and 30 $\mu\text{m}$ , Veilleux et al. 2013). By applying the correlation of  $SFR(M_{\odot}, \text{yr}^{-1}) = 4.5 \pm 1.4 \times 10^{44} L_{\text{FIR}}(\text{erg s}^{-1})$  (Kennicutt 1998), the  $SFR$  estimated from the FIR dust emission is  $SFR_{\text{FIR}} = 190 \pm 90 M_{\odot} \text{yr}^{-1}$ . Since the  $SFR$  value is more reliably determined based on the FIR luminosity rather than on the PAH emission, it will be applied in the follow-up discussion.

Similar to the optical emission lines, it is reported that the MIR [Ne III] and [Ne V] emission lines of F11119+3257 are also significantly blueshifted (Spoon et al. 2009). As described in §3.2.3, we apply the same method in retrieving the [Ne III]  $\lambda 15.56\mu\text{m}$  and [Ne V]  $\lambda 14.32\mu\text{m}$  OELs (Figure 7.2, 7.3). The MIR [Ne III] and [Ne V] OELs show a similar two-component profiles to their optical counterparts, their fluxes are also calculated and listed in Table 3.

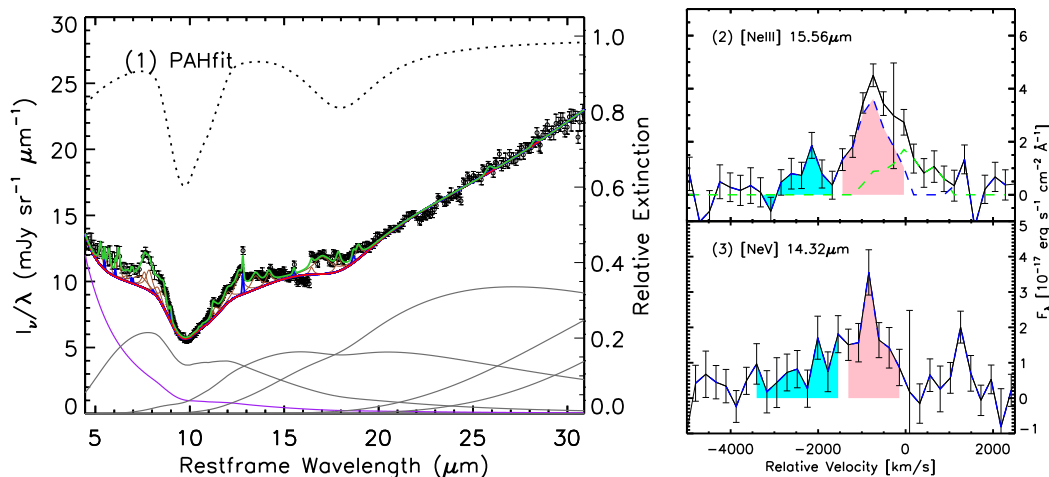


Fig. 7.— Panel (1): PAHfit model of the Spitzer IRS spectrum of F11119+3257. The black circles with error bars are rebinned Spitzer IRS data of F11119+3257. Best-fit model is shown with green solid line, combined thermal dust continuum (grey solid lines) and stellar component (purple solid line) is in red solid lines. PAH emissions and other ionic/atomic/molecular lines are presented with brown and blue solid lines respectively. All components are reddened with the fully mixed extinction curve (dotted black line, with an axis at the right). After subtracting local continuum, the emission line profiles (black solid lines) of [Ne III]  $\lambda 15.56\mu\text{m}$  and [Ne V]  $\lambda 14.32\mu\text{m}$  are displayed in panel (2) and panel (3) respectively. The “NEL” (green dashed lines), the fast OEL (cyan shaded regions), and the slow OEL components (pink shaded regions) are marked in the same way as in Figure 5.

## 4. DISCUSSION

### 4.1. Properties of the Quasar

Similar to some previous reports, the SED modeling in §3.1 reveals that F11119+3257 is heavily obscured in the optical and NIR. Thus the intrinsic optical-NIR fluxes are much stronger than we observed and dereddening needs to be carried out before estimating luminosity and ionizing fluxes. The BH mass of F11119+3257 has been evaluated in some previous sample studies. One estimate is  $10^{7.2}M_{\odot}$  by Kawakatu et al. (2007), which is based on directly observed monochromatic luminosity at 5100Å and the width of the BELs. The other estimate is  $10^{9.44}M_{\odot}$  by Veilleux et al. (2009), which is based on the  $H$  band luminosity. In sample studies, it is a reasonable assumption that the accretion rate is similar among AGNs when BH mass is estimated according to luminosity. However for special AGNs like NLS1s, BH masses estimated with this method tend to be too larger as Eddington ratio of NLS1s are intrinsically higher than that of typical AGNs. Thus it is more reliable to estimate BH mass of F11119+3257 based on scaling relation between the BH and the BELR. Such an empirical correlations are established mostly based on extinction-free AGNs. However, the extinction toward F11119+3257 is likely to be among the strongest of the “type 1” AGNs studied in Kawakatu et al. (2007). Unlike sample studies which did not focus mainly on individual objects, we think it is necessary to re-estimate the BH mass after extinction correction in this paper. Applying the relation of the BH mass with the  $H\alpha$  line width and the extinction-free luminosity (Greene and Ho 2005), we estimate that  $M_{\text{BH}} = 1.0_{-0.2}^{+0.4} \times 10^8 M_{\odot}$ . Considering the quasar luminosity of  $L_{\text{bol}} = 10^{12.61} L_{\odot} \approx 1.6 \times 10^{46} \text{ erg s}^{-1}$  (Veilleux et al. 2013), an Eddington ratio of  $\frac{L_{\text{bol}}}{L_{\text{Edd}}} \approx 1.0$  is found, which is typical among NLS1s. If the MF87 (Mathews & Ferland 1987) SED of active galaxies is assumed, the incident rate of ionizing photons is  $Q_{\text{H}} \approx 1.6 \times 10^{56} \text{ s}^{-1}$ .

### 4.2. Physical Condition of Outflow Material

Since all the absorption lines lie in a similar velocity range, the blueshifted Na I  $\lambda\lambda$  5891,5897, He I\*  $\lambda$  10830 and Ca II  $\lambda$ 3934 mini-BALs are very probably associated with the OH outflow. Photo-ionization properties of the outflow gas can be constrained with the measured ionic (Ca II  $\lambda$ 3934), atomic (Na I  $\lambda\lambda$  5891,5897 and the metastable He I\*  $\lambda$  10830) column densities. An attempt to investigate physical properties of the outflow material is thus conducted with *CLOUDY* (c13.03; Ferland 1998) photo-ionization simulations. Given that the line profiles of the broad absorptions are rather complex, the actual gas cloud is likely to be multi-phased. However, constrained by the insufficient data quality and limited number of lines being detected, only 1-zone photo-ionization simulation is conducted. The general physical property of the outflow gas could be estimated if simulations converge.

The MF87 AGN SED is assumed as the incident radiation field for the outflowing material in *CLOUDY* simulations. Since atomic sodium is the most robust column density measurements available, we set up the stopping criteria (thickness of the cloud) for *CLOUDY* to be  $N_{\text{Na}^0} = 10^{13.7} \text{ cm}^{-2}$ . With the detection of molecular absorption, the incident radiation field cannot be too strong, or molecules would be destroyed. And a moderate number density of atoms is required to allow molecules to grow. 2-dimensional grids of *CLOUDY* simulations with ionization parameter  $U$  ranging from  $10^{-4}$  to 1 and hydrogen number density  $n_{\text{H}}$  ranging from  $1 \text{ cm}^{-3}$  to  $10^{10} \text{ cm}^{-3}$  are carried out. Four discrete metallicity values are assumed, i.e.  $0.3 Z_{\odot}$ ,  $1.0 Z_{\odot}$ ,  $3.2 Z_{\odot}$ , and  $10.0 Z_{\odot}$ , where  $Z_{\odot}$  stands for solar abundance. Since we found heavy extinction in F11119+3257, dust depletion should be taken into account when dealing with gas-phase absorption. We assume a depletion pattern of the Galactic warm cloud (Welty et al, 1999), which happens to approximate

the depletion pattern observed in several quasar proximate dusty absorbers (Pan et al. 2017; Ma et al. 2017). The corresponding depletion of Sodium and Calcium are  $-0.4 dex$  and  $-2.0 dex$  respectively. Based on the incident radiation ( $Q_H \approx 1.6 \times 10^{56} s^{-1}$ ) and the definition of ionization parameter  $U = \frac{Q_H}{4\pi R^2 n_H c}$ , the distance  $R$  of the absorber can be figured when  $U$  and  $n_H$  are specified (thin dotted lines in Figure 8-9). The matched region between model prediction and measured column densities are shown in Figure 8-9. The column density measurement  $N_{Ca^+} < 10^{14.0} cm^{-2}$  (thick dashed line in Figure 8-9) puts a constrain of  $U \lesssim 10^{-1}$ , if a common ISM number density of  $n_H < 10^6 cm^{-3}$  is assumed. And the lower limit of log  $N_{He^0(2^3S)}$  requires a distance of  $R < 10 kpc$  and a number density of  $n_H \gtrsim 10^2 cm^{-3}$  in the parameter space investigated. In addition, if gas-to-dust ratio of the dust-rich MW (Bohlin et al. 1978) or the relatively dust-deficient SMC (Martin et al. 1989) are assumed, the Hydrogen column density corresponding to the measured extinction  $E_{B-V} = 1.18$  is  $N_H(SMC) = 10^{22.7} cm^{-2}$  and  $N_H(MW) = 10^{21.8} cm^{-2}$  respectively (thick dash-dotted lines in Figure 8-9). For typical ISM with  $n_H < 10^6 cm^{-3}$ , the Hydrogen column density of  $N_H(SMC) = 10^{22.7} cm^{-2}$  do not overlap with the column density measurements of other species in the parameter space. Thus the MW gas-to-dust ratio is preferred, indicating the outflow gas is relatively dust-rich and has a relatively high metallicity. On the other hand,  $N_H(MW) = 10^{21.8} cm^{-2}$  only overlap with other elemental column densities in parameter space with metallicities of  $Z \in [0.3, 3.2]Z_\odot$ . Briefly speaking, these column density measurements suggests that the outflow material posits at a distance of kilo-parsec scale toward the central engine, similar to previous estimates based on the OH mini-BAL (Tombsesi et al. 2015).

On the other hand, the blueshifted emission lines are also detected in a similar velocity range (Table 2). Similar to the outflow in SDSS J1634+2049 reported by Liu et al. (2016), such a resemblance in speed suggests that these blueshifted emission lines probably originate from the absorption line outflow. We therefore compare the predicted emission line ratios of the *CLOUDY* simulations with the observed fluxes of the outflow emission lines. There appear to be two distinct OEL component, the fast OEL and the slow OEL (§3.2.3). Their line ratios are quite different, and may rise from different region of the outflow gas. Thus these two OEL systems are compared separately with the mini-BAL system. The strongest OEL, [O III]  $\lambda 5007$ , is used as a normalization to the other emission lines. The matched regions of these line ratios are marked with colored stripes in Figure 8 (slow OEL) and Figure 9 (fast OEL). And since [Ne III]  $\lambda 3869\text{\AA}$  is probably contaminated by He I\* absorption (§3.2.3), the relatively weaker [Ne III]  $\lambda 3968\text{\AA}$  is investigated in stead in the photo-ionization diagnoses. We found that for the component with higher fluxes, which more likely represents the bulk of the outflow material (i.e. slow OEL), a solution for the emission line ratios can only be found at the solar abundance ( $Z = Z_\odot$ ; Figure 8.2). The resulted photo-ionization parameters are  $\log U \sim -2.0$ ,  $\log n_H \sim 2.7$ ,  $R \sim 3.1 kpc$  and  $\log N_H \sim 21.6 cm^{-2}$  (red diamond in Figure 8). For the fast OEL component (Figure 8), if solar abundance is adopted, a best-fit model is found with  $\log U \sim -1.6$ ,  $\log n_H \sim 2.5$ ,  $R \sim 2.3 kpc$  and  $\log N_H \sim 21.8 cm^{-2}$  (black star in Figure 8-9). The corresponding gas-to-dust ratios are close to MW, consistent with the assumption of solar abundance. After a brief comparison between the best-fit parameters of the fast and the slow OEL component, we find that they are generally consistent with each other. In the meantime, model results suggest that the fast OEL component might be closer to the central illuminant, and endures a higher incident radiation, which could shield the material more distant in the outflow gas and allow molecules to grow.

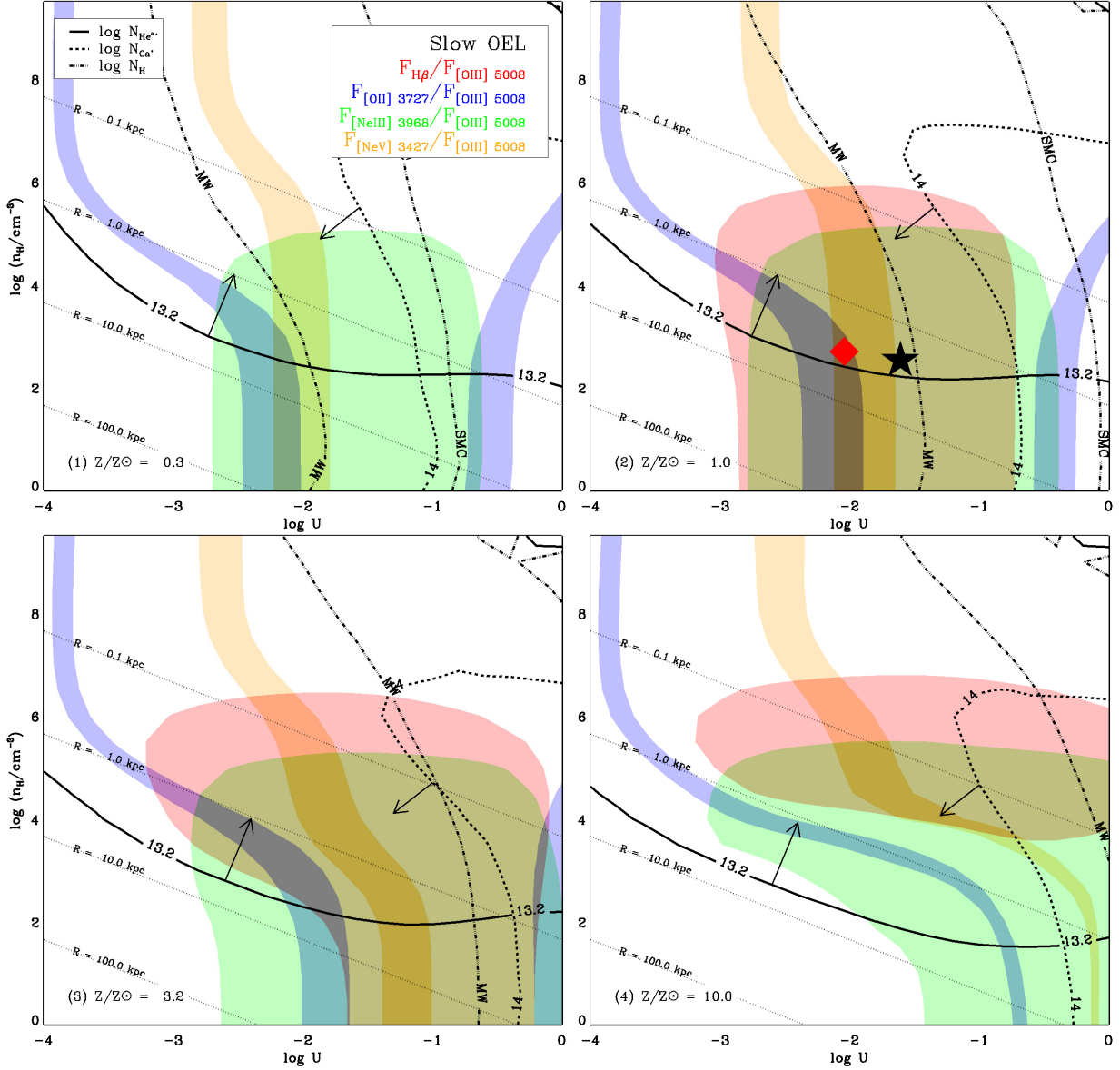


Fig. 8.— *CLOUDY* simulations versus the measured mini-BAL column densities and the slow Outflow Emission Line flux ratios are shown. From panel (1) to panel (4), the assumed metallicity are  $0.3Z_{\odot}$ ,  $1Z_{\odot}$ ,  $3.2Z_{\odot}$ , and  $10Z_{\odot}$  respectively. Colored stripes correspond to matched emission line ratios between simulations and measurements. The thick dash-dotted lines are Hydrogen column densities with assumption of gas-to-dust ratios of MW or SMC. In panel (2) (solar abundance), we mark the best guess of the photoionization parameters with a red diamond, which is around  $\log U \sim -2.0$ ,  $\log n_{\text{H}} \sim 2.7$  and  $R \sim 3.1$  kpc. And the black star is the best-guess for the fast Outflow Emission Lines in Figure-9.

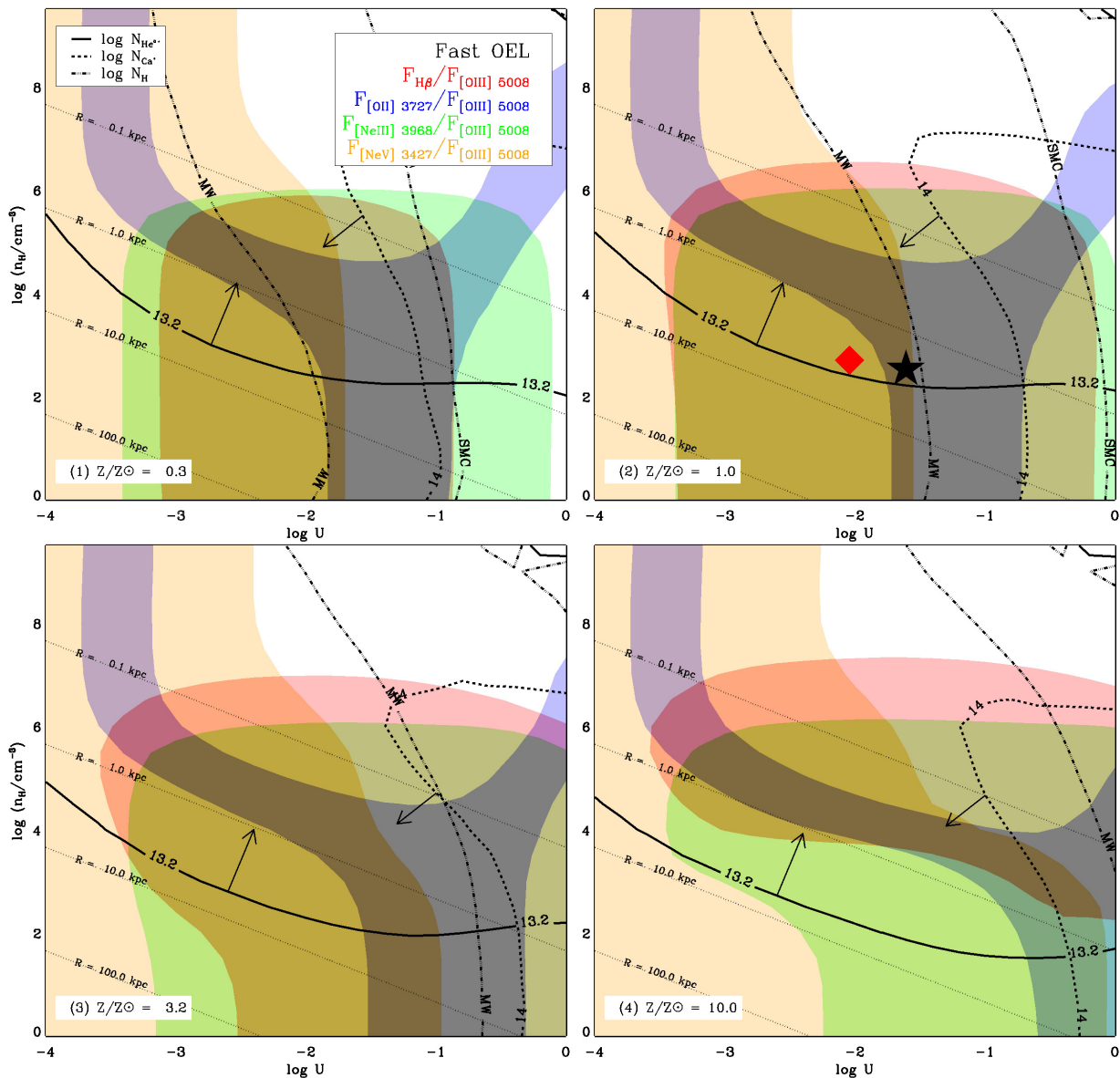


Fig. 9.— Similar to Figure 8, *CLOUDY* simulations versus the measure mini-BAL column densities and the fast Outflow Emission Line flux ratios are shown. In panel (2) (solar abundance), we mark the best guess of photo-ionization parameters with a black star, which is around  $\log U \sim -1.6$ ,  $\log n_{\text{H}} \sim 2.5$  and  $R \sim 2.3$  kpc. And the red diamond is the best-guess for the slow Outflow Emission Lines in Figure-9.

Since the modeled physical parameters of the fast and the slow OEL components are similar, the two sets of results are considered together in estimating the physical condition of the outflow gas. The thickness of outflowing cloud is estimated to be  $\Delta R = N_{\text{H}}/n_{\text{H}} \in [2, 12]$  pc, much smaller than the estimated distance  $R$ . Thus the bulk of the outflowing material follows roughly a geometry of partially filled thin shell ( $\Delta R/R \ll 1$ ). Following Borguet et al. (2012), the mass-flow rate ( $\dot{M}$ ), momentum flux ( $\dot{P}$ ), and kinetic luminosity ( $\dot{E}_k$ ) can

be derived:  $\dot{M} = 4\pi R\Omega\mu m_p N_H v$ ,  $\dot{P} = \dot{M}v$ ,  $\dot{E}_k = \frac{1}{2}\dot{M}v^2$ .  $\Omega$  is the global covering factor of the outflow, and  $m_p$  is the proton mass. The flux weighted average velocity of the outflow emission lines are  $v \in [-1449, -810]$  km s<sup>-1</sup> for different lines (Table 3). According to *CLOUDY* simulations, distance and column density are in ranges of  $R \sim 2.3$ -3.1 kpc and  $N_H \sim 10^{21.6-21.8}$  cm<sup>-2</sup>. Solar abundance is favoured, which corresponds to a mean atomic mass per proton of  $\mu = 1.4$ . As demonstrated in Liu et al. (2016), strong extinction can lead to large uncertainty in calculating global covering fraction. In the case of F11119+3257, ratio between observed  $EW([\text{O III}])$  and *CLOUDY* predictions suggests  $0.1\% \lesssim \Omega \lesssim 10\%$ . The uncertainty is too large for a reasonable estimation of the energetics of the outflow. Therefore, the relatively more reliable covering factor estimation based on Herschel OH spectrum  $C_f(\text{OH}) = 0.20 \pm 0.05$  is adopted (Tombesi et al. 2015). The kinematics of the outflow material is then:  $\dot{M} \sim 230$ -730  $M_\odot \text{yr}^{-1}$ , the momentum flux is  $\dot{P} \sim 2.2$ -12.7  $L_{\text{AGN}}/c$  and the kinetic luminosity is  $\dot{E}_k \sim 10^{43.6-44.8} \sim 0.003 - 0.030 L_{\text{AGN}}$ . The estimated distance of the outflow is consistent with recent results based on spatially resolved observations of the CO outflow emission line (at a scale of  $\sim 7$  kpc; Veilleux et al. 2017).

### 4.3. Star Formation in the Host Galaxy

During the analysis of the emission lines, the narrow Paschen emission (§3.2.2) discovered in only Pa $\alpha$  caught our interest. Such narrow emission lines usually come from the NELR of the quasar or from the H II regions around newly formed O stars that traces star formation activity in the host galaxy. The Paschen emission is of only half the width of the other NELs, which makes it unlikely originated from the NELR. On the other hand, if we apply the heavy extinction  $A_H > 2.1$  (corresponding to  $E_{B-V} > 3.7$ ) of the Paschen emissions to the NELs we observe, the extinction-free luminosity of the  $[\text{O II}] \lambda 3727$  is then  $L_{[\text{O II}] \lambda 3727} > 5.8 \times 10^{47} \text{ergs}^{-1}$ , even larger than the bolometric luminosity of the quasar. Thus the Paschen emissions are unlikely NELs of the quasar, which makes star formation region the most plausible origin. Assuming a case-B line ratio for the anomalous Hydrogen emission lines, the luminosity of H $\alpha$  associated with the narrow Paschen component after extinction correction is  $L_{\text{H}\alpha \text{ peak}} > 1.7 \times 10^{43} \text{ergs}^{-1}$ . An  $SFR$  of  $SFR_{\text{Pa}\alpha \text{ peak}} > 130 M_\odot \text{yr}^{-1}$  is obtained according to the relation  $SFR = L_{\text{H}\alpha} / 1.26 \times 10^{41} \text{ergs}^{-1}$  (Kennicutt 1998). Since extinction is tightly correlated with  $SFR$  as studied in star-forming galaxies (Xiao et al. 2012), the heavy extinction to the narrow Paschen emission is expected as the star formation rate is high. The lower limit of  $SFR$  based on the anomalous Paschen emission is of a similar order of our previous estimates based on FIR emission ( $SFR_{\text{FIR}} = 190 \pm 90 M_\odot \text{yr}^{-1}$ ), and the extinction to the star formation region is also present in the Spitzer spectrum as the prominent silicate absorption. Detection of the narrow Pa $\alpha$  emission indicates that spectroscopy of the IR Hydrogen emission lines can be powerful probes to the star-burst regions that are usually heavily obscured. With the launch of JWST, the narrow Brackett (1.46-4.05  $\mu\text{m}$ ) and Pfund (2.28-7.46  $\mu\text{m}$ ) emissions from H II region can be observed in detail, which will help to precisely measure the obscuration and spatial distribution of the star formation region.

In the previous section, we show that large amount of kinetic energy is injected into the host galaxy in the form of powerful outflows. Such strong galactic-scale feedback in F11119+3257 can be responsible for the violent star formation activity, or regulate star formation processes. On the other hand, stellar feedback at high  $SFR$  can also play a significant role in forming outflows. The simulation in Biernacki & Teyssier (2018) shows that, in a dark matter hole of the mass around  $2 \times 10^{12} M_\odot$ , continuous  $SFR$  at  $\sim 100 M_\odot \text{yr}^{-1}$  along can launch massive ( $\sim 20 M_\odot \text{yr}^{-1}$ ) molecular outflow at a scale of  $\sim 20$  kpc. At  $\sim 190 M_\odot \text{yr}^{-1}$ , the more violent  $SFR$  in F11119+3257 are capable of contributing significantly to the massive molecular outflow been observed. According to some previous findings (Davé et al. 2011, etc), however, the fast wind speed of

the outflow ( $\sim 1000\text{km s}^{-1}$ ) in F11119+3257 can only be caused by AGN feedback. Given the power and scale of the outflow, it must interact with the violent star formation been observed. Detailed processes of the interactions need follow-up spatially-resolved observations and simulations to reveal.

#### 4.4. Implications of MIR Emission Lines

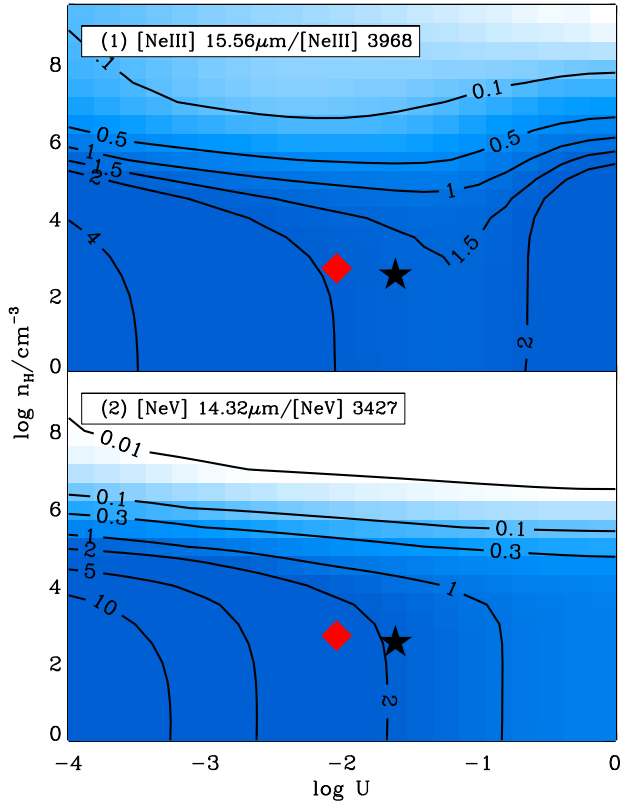


Fig. 10.— The emission line ratios of [Ne III]  $\lambda 15.56\mu\text{m}/[\text{Ne III}] \lambda 3968$  (upper panel) and [Ne V]  $\lambda 14.3\mu\text{m}/[\text{Ne V}] \lambda 3427$  (lower panel) predicted by the *CLOUDY* simulations with solar abundance are shown. The predicted line ratios for the OELs (around the red squares and black stars) are [Ne III]  $\lambda 15.56\mu\text{m}/[\text{Ne III}] \lambda 3968$ (*CLOUDY*) $\approx 1.8$  and [Ne V]  $\lambda 14.32\mu\text{m}/[\text{Ne V}] \lambda 3427$ (*CLOUDY*) $\approx 2.0$ .

As shown in section 3.4, prominent blueshifted MIR Neon lines are detected in F11119+3257. It is an interesting fact that the line profile of the MIR Neon emission lines are similar to optical Neon lines, suggesting that both of them should rise from the outflow gas. A comparison study of the optical and the MIR Neon lines can probably implicate physical properties of the emission line region. Given the large difference in wavelength between the optical ( $\sim 0.4\mu\text{m}$ ) and the MIR ( $\sim 15\mu\text{m}$ ) Neon lines, potential extinction to the outflow gas can be investigated since extinction at the optical bands are much stronger than in the MIR. Heavy extinction is found for the both the continuum and the BELs of F11119+3257, the OELs can also be obscured. The observed OEL fluxes ratios are [Ne III]  $\lambda 15.56\mu\text{m}/[\text{Ne III}] \lambda 3968$ (observed) $\approx 13.7$

and  $[\text{Ne V}] \lambda 14.32\mu\text{m}/[\text{Ne V}] \lambda 3427(\text{observed})\approx 16.8$ . However, the predicted emission line ratios for the OELs by *CLOUDY* simulations are only around  $[\text{Ne III}] \lambda 15.56\mu\text{m}/[\text{Ne III}] \lambda 3968(\text{CLOUDY})\approx 1.8$  and  $[\text{Ne V}] \lambda 14.32\mu\text{m}/[\text{Ne V}] \lambda 3427(\text{CLOUDY})\approx 2.0$  (Figure 10). The relatively lower fluxes of the blueshifted Neon lines at the optical bands are very likely caused by dust extinction given the association of the outflow with the obscuring dust. If the cubic extinction curve for the continuum is applied, an extinction of  $E_{B-V}^{\text{OELR}} \approx 0.5$  for the outflow can be derived. This value is lower than the extinction to the BELR, consistent with the changing profiles of the Hydrogen emission lines been observed (OELs become stronger at shorter wavelengths as compared to BELs; §3.2.2).

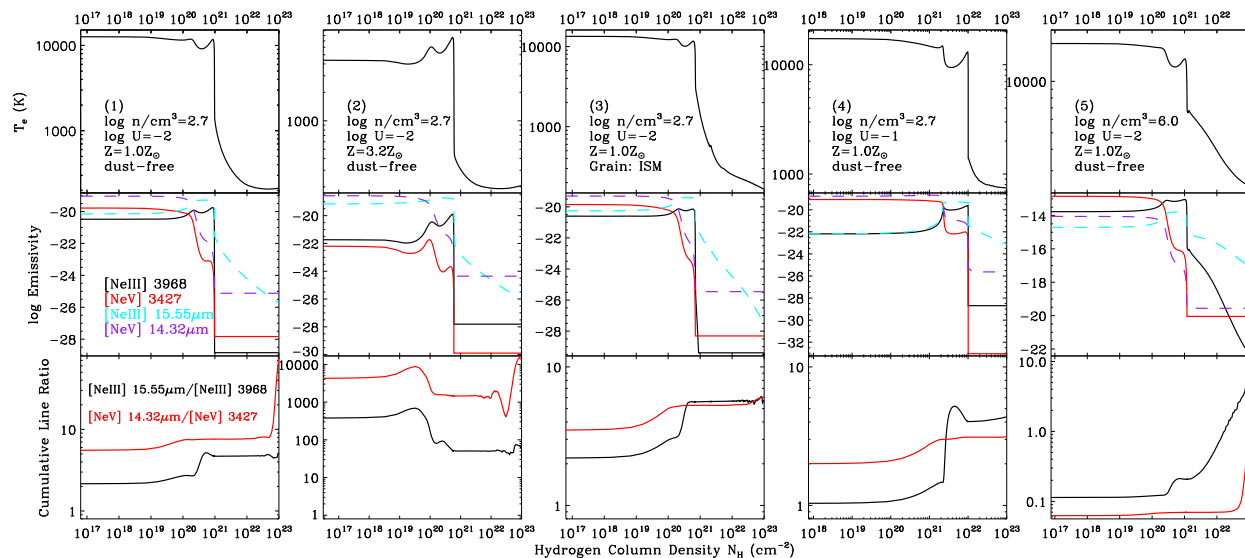


Fig. 11.— Emissivity structure of Neon lines in clouds illuminated by AGN predicted by *CLOUDY* simulations. The structure of electron temperature ( $T_e$ ) is in the upper panels, line emissivities are in the middle panels and cumulative line ratios are in the lower panels. The differences between panel (1) and other panels are: (2) metallicity, (3) presence of dust, (4), ionization parameter, (5) number density.

On the other hand, the MIR-to-optical Neon line intensity ratios can also be affected by factors other than extinction as upper levels of these transitions are different. *CLOUDY* simulations of emissivity structures of these Neon lines in clouds illuminated by AGN reveal some clue. Thick gas slabs ( $\log N_{\text{H}}/\text{cm}^{-2} = 23$ ) with various physical conditions are assumed in *CLOUDY* modelings, and results are shown in Figure 11.1-5 respectively. The structures of temperature ( $T_e$ ), line emissivities and cumulative line ratios are in the upper, middle and lower panels respectively. First of all, as number density rises from  $n_{\text{H}} = 10^{2.7}\text{cm}^{-3}$  (Figure 11.1) to about  $n_{\text{H}} = 10^6\text{cm}^{-3}$  (around the critical density of these Neon lines; Figure 11.5), the line emissivities rise dramatically, and the cumulative line ratios show an entirely different pattern. Beside number density, it is clear that the emissivity and line ratios are mainly determined by temperature of the gas, which is affected by facts like ionization parameter  $U$  (Figure 11.1 v.s. Figure 11.4), Metallicity  $Z$  (Figure 11.1 v.s. Figure 11.2), and the presence of dust (Figure 11.1 v.s. Figure 11.3). In the case of the outflow gas in F11119+3257, the observed line ratios of  $[\text{Ne III}] \lambda 15.56\mu\text{m}/[\text{Ne III}] \lambda 3968(\text{observed})\approx 13.7$  and  $[\text{Ne V}] \lambda 14.32\mu\text{m}/[\text{Ne V}] \lambda 3427(\text{observed})\approx 16.8$  are hard to be explained as caused by the change of the physical conditions as shown in the figures. The variation of neither  $n_{\text{H}}$ ,  $U$ , or dust content can boost the MIR/optical

Neon ratios to be over 10. A higher metallicity (Figure 11.2) though, can result in a  $[\text{Ne III}] \lambda 15.56\mu\text{m}/[\text{Ne III}] \lambda 3968$  ratio similar to our observation, but the predicted  $[\text{Ne V}] \lambda 14.32\mu\text{m}/[\text{Ne V}] \lambda 3427$  intensity ratio becomes much too large. Therefore the case of F11119+3257 implicates that comparison study of MIR and optical Neon lines can provide additional diagnoses to the physical conditions (e.g. extinction) of the emission line regions of galaxies.

## 5. SUMMARY AND PROSPECT

In this paper, we carry out a comprehensive study of the continuum, emission lines, and absorption lines of the fast molecular outflow candidate, a ULIRG + partially-obscured NLS1 IRAS F11119+3257. A systemic redshift of  $z = 0.18966 \pm 0.00006$  is determined by modeling low-ionization narrow emission lines. And significant dust extinction at  $E_{B-V} \sim 1.18$  is found for both the continuum and the BELs. The dereddened optical spectrum reveals a powerful AGN with a black hole mass of  $M_{\text{BH}} = 1.0^{+0.4}_{-0.2} \times 10^8 M_{\odot}$ , which accretes at around the Eddington rate of  $\frac{L_{\text{bol}}}{L_{\text{Edd}}} \approx 1$ . Broad absorption lines from ions (Ca II  $\lambda 3934$ ), neutral atoms (Na I  $\lambda\lambda 5891, 5897$  and the metastable He I\*  $\lambda 10830$ ) are detected at the velocities ( $\sim -1000 \text{ km s}^{-1}$ ) similar to that of the molecular OH  $119\mu\text{m}$  mini-BAL. Photo-ionization diagnosis of the ionic, atomic, and molecular lines found that the mini-BAL outflows are at kilo-parsec scale, consistent with previous reports. At similar speeds to the mini-BAL, a blueshifted emission line system is identified in several ions ( $[\text{O III}] \lambda\lambda 4959, 5007$ ,  $[\text{O II}] \lambda 3727$ ,  $[\text{Ne III}] \lambda 3869$ , and  $[\text{Ne V}] \lambda 3427$ ) and atomic Hydrogen ( $\text{H}\alpha$ ,  $\text{H}\beta$  and  $\text{H}\gamma$ ). The similarity in kinetic properties between the blueshifted emission and absorption lines suggests that they could be associated. The blueshifted emission lines are broad, and are divided into two components: the slow OEL component ( $(-1500, 0) \text{ km s}^{-1}$ ) and the relatively high-ionization fast OEL component ( $[-3500, -1500] \text{ km s}^{-1}$ ). After inspecting the predicted emission line ratios of the mini-BAL outflows, we find that it will match the line ratios of the fast and slow OEL components if solar abundance and a dust-to-gas ratio similar to MW are assumed. And the physical conditions of the fast and slow OEL components are similar even they differ largely in their line ratios. These results indicate that the OELs are very likely originated from the mini-BAL outflows. A joint analysis based on these ionic/atomic/molecular mini-BALs and OELs reveals the position ( $R \sim 3 \text{ kpc}$  from the black hole) and physical properties ( $n_{\text{H}} \sim 10^{2.6} \text{ cm}^{-3}$  and  $N_{\text{H}} \sim 10^{21.7} \text{ cm}^{-2}$ ) of the galactic scale outflow. Further more, the mass-flow rate ( $\dot{M} \sim 230 - 730 M_{\odot} \text{ yr}^{-1}$ ), the momentum flux ( $\dot{P} \sim 2.2 - 12.7 L_{\text{AGN}}/c$ ) and the kinetic luminosity ( $\dot{E}_k \sim 10^{43.6-44.8} \sim 0.003 - 0.030 L_{\text{AGN}}$ ) are obtained. In addition, the presence of the blueshifted  $[\text{Ne III}]$  and  $[\text{Ne V}]$  emission lines in the MIR provides chances to investigate additional properties of the outflow gas, and an extinction of  $E_{B-V} \sim 0.5$  is inferred for the outflow region. Besides, we found that the Paschen emission line in F11119+3257 is unique, in which a very narrow ( $FWHM_{\text{Pa}\alpha \text{ peak}} = 260 \pm 20 \text{ km s}^{-1} < FWHM_{\text{NEL}}/2$ ) emission line component is found only in  $\text{Pa}\alpha$ . By checking this Paschen emission line component in  $\text{Pa}\alpha$  and  $\text{Pa}\beta$ , a heavy extinction at  $A_{\text{H}} > 2.1$  (corresponding to  $E_{B-V} > 3.7$ ) is found. The most plausible explanation to this anomalous Paschen emission is that it comes from heavily obscured star formation, and a lower limit of  $SFR_{\text{Pa}\alpha \text{ peak}} > 130 M_{\odot} \text{ yr}^{-1}$  is obtained. The result is of a similar order of the estimates inferred from FIR emissions ( $SFR_{\text{FIR}} = 190 \pm 90 M_{\odot} \text{ yr}^{-1}$ ). This shows that Hydrogen emission lines in the IR (Paschen series, Bracket series, etc.) can be powerful probes to the star formation regions even if they are heavily obscured.

With such a massive molecular outflow and high  $SFR$ , F11119+3257 is among the best laboratory to study both the formation of galactic-scale outflows and the outflow-starformation interactions. At a physical scale of  $\sim 3 \text{ kpc}$  ( $\sim 1''$  for  $z = 0.18966$ ), the emission lines from both the galactic-scale outflow and the star formation region can be spatially resolved by the next-generation telescopes like JWST. The spatially and

spectrally resolved observations will enable a clear view of the outflow and the star formation processes, and their interactions.

We are thankful to the helpful comments about starformation rate estimation and the implications of MIR Neon emission lines from an anonymous referee on this paper. This work is supported by the National Natural Science Foundation of China (NSFC-11573024, 11903029, 11473025, 11421303) and the National Basic Research Program of China (2013CB834905). WL acknowledges supports from the Natural Science Foundation of China grant (NSFC-11703079) and the "Light of West China" Program of Chinese Academy of Sciences (CAS). PJ is supported by the National Natural Science Foundation of China (NSFC-11973037) and HW is supported by the Natural Science Foundation of China (NSFC-11890693). We acknowledge the use of the Hale 200-inch Telescope at Palomar Observatory through the Telescope Access Program (TAP), as well as the archival data from the SDSS, 2MASS, Catalina, WISE surveys and Spitzer space telescope. TAP is funded by the Strategic Priority Research Program, the Emergence of Cosmological Structures (XDB09000000), National Astronomical Observatories, Chinese Academy of Sciences, and the Special Fund for Astronomy from the Ministry of Finance. Observations obtained with the Hale Telescope at Palomar Observatory were obtained as part of an agreement between the National Astronomical Observatories, Chinese Academy of Sciences, and the California Institute of Technology. Funding for SDSS-III has been provided by the Alfred P. Sloan Foundation, the Participating Institutions, the National Science Foundation, and the U.S. Department of Energy Office of Science. The SDSS-III website is <http://www.sdss3.org/>

## REFERENCES

- Abazajian, K. N., Adelman-McCarthy, J. K., Agüeros, M. A., et al. 2009, *ApJS*, 182, 543
- Ahn, C. P., Alexandroff, R., Allende Prieto, C., et al. 2014, *ApJS*, 211, 17
- Biernacki, P., & Teyssier, R. 2018, *MNRAS*, 475, 5688
- Bohlin, R. C., Savage, B. D., & Drake, J. F. 1978, *ApJ*, 224, 132
- Borguet, B. C. J., Edmonds, D., Arav, N., Dunn, J., & Kriss, G. A. 2012, *ApJ*, 751, 107
- Chamberlain, C., & Arav, N. 2015, *MNRAS*, 454, 675
- Clements, D. L., Dunne, L., & Eales, S. 2010, *MNRAS*, 403, 274
- Cushing, M. C., Vacca, W. D., & Rayner, J. T. 2004, *PASP*, 116, 362
- Davé, R., Oppenheimer, B. D., & Finlator, K. 2011, *MNRAS*, 415, 11
- Dong, X., Wang, T., Wang, J., et al. 2008, *MNRAS*, 383, 581
- Dong, X.-B., Wang, J.-G., Ho, L. C., et al. 2011, *ApJ*, 736, 86
- Drake, A. J., Djorgovski, S. G., Mahabal, A., et al. 2009, *ApJ*, 696, 870
- Dunn, J. P., Bautista, M., Arav, N., et al. 2010, *ApJ*, 709, 611
- Fabian, A. C. 2012, *ARA&A*, 50, 455
- Farrah, D., Bernard-Salas, J., Spoon, H. W. W., et al. 2007, *ApJ*, 667, 149

- Ferland, G. J., Korista, K. T., Verner, D. A., et al. 1998, *PASP*, 110, 761
- Ferrarese, L., & Merritt, D. 2002, arXiv e-prints, astro-ph/0206222
- Fitzpatrick, E. L. 1986, *AJ*, 92, 1068
- Fitzpatrick, E. L., & Massa, D. 2007, *ApJ*, 663, 320
- Glikman, E., Helfand, D. J., & White, R. L. 2006, *ApJ*, 640, 579
- Glikman, E., Helfand, D. J., White, R. L., et al. 2007, *ApJ*, 667, 673
- Greene, J. E., Zakamska, N. L., & Smith, P. S. 2012, *ApJ*, 746, 86
- Greene, J. E., & Ho, L. C. 2005, *ApJ*, 630, 122
- Higdon, S. J. U., Armus, L., Higdon, J. L., Soifer, B. T., & Spoon, H. W. W. 2006, *ApJ*, 648, 323
- Hummer, D. G., & Storey, P. J. 1987, *MNRAS*, 224, 801
- Jiang, P., Zhou, H., Ji, T., et al. 2013, *AJ*, 145, 157
- Johnson, H. L., & Morgan, W. W. 1953, *ApJ*, 117, 313
- Kawakatu, N., Imanishi, M., & Nagao, T. 2007, *ApJ*, 661, 660
- Kennicutt, R. C., Jr. 1998, *ARA&A*, 36, 189
- Kim, D.-C., & Sanders, D. B. 1998, *ApJS*, 119, 41
- Komossa, S., Voges, W., Xu, D., et al. 2006, *AJ*, 132, 531
- Komossa, S., Xu, D., Zhou, H., Storchi-Bergmann, T., & Binette, L. 2008, *ApJ*, 680, 926-938
- Kormendy, J., & Ho, L. C. 2013, *ARA&A*, 51, 511
- Landt, H., Bentz, M. C., Ward, M. J., et al. 2008, *ApJS*, 174, 282-312
- Law, N. M., Kulkarni, S. R., Dekany, R. G., et al. 2009, *PASP*, 121, 1395
- Lebouteiller, V., Barry, D. J., Spoon, H. W. W., et al. 2011, *ApJS*, 196, 8
- Li, Z., Zhou, H., Hao, L., et al. 2015, *ApJ*, 812, 99
- Liu, W.-J., Zhou, H., Ji, T., et al. 2015, *ApJS*, 217, 11
- Liu, W.-J., Zhou, H.-Y., Jiang, N., et al. 2016, *ApJ*, 822, 64
- Ma, J., Ge, J., Zhao, Y., et al. 2017, *MNRAS*, 472, 2196
- Martin, N., Maurice, E., & Lequeux, J. 1989, *A&A*, 215, 219
- Mathews, W. G., & Ferland, G. J. 1987, *ApJ*, 323, 456
- Moshir, M., & et al. 1990, *IRAS Faint Source Catalogue, version 2.0 (1990)*,
- etzer, H., Lutz, D., Schweitzer, M., et al. 2007, *ApJ*, 666, 806

- Pan, X., Zhou, H., Ge, J., et al. 2017, *ApJ*, 835, 218
- Pâris, I., Petitjean, P., Ross, N. P., et al. 2017, *A&A*, 597, A79
- Prevot, M. L., Lequeux, J., Prevot, L., Maurice, E., & Rocca-Volmerange, B. 1984, *A&A*, 132, 389
- Richards, G. T., Kruczek, N. E., Gallagher, S. C., et al. 2011, *AJ*, 141, 167
- Riffel, R., Rodríguez-Ardila, A., & Pastoriza, M. G. 2006, *A&A*, 457, 61
- Rupke, D. S., Veilleux, S., & Sanders, D. B. 2005, *ApJ*, 632, 751
- Rupke, D. S. N., & Veilleux, S. 2013, *ApJ*, 768, 75
- Savage, B. D., & Sembach, K. R. 1991, *ApJ*, 379, 245
- Scannapieco, E., & Oh, S. P. 2004, *ApJ*, 608, 62
- chlaflly, E. F., & Finkbeiner, D. P. 2011, *ApJ*, 737, 103
- Sijacki, D., Springel, V., Di Matteo, T., & Hernquist, L. 2007, *MNRAS*, 380, 877
- Skrutskie, M. F., Cutri, R. M., Stiening, R., et al. 2006, *AJ*, 131, 1163
- Smith, J. D. T., Draine, B. T., Dale, D. A., et al. 2007, *ApJ*, 656, 770
- Spoon, H. W. W., & Holt, J. 2009, *ApJ*, 702, L42
- Storey, P. J., & Zeppen, C. J. 2000, *MNRAS*, 312, 813
- Sturm, E., Lutz, D., Verma, A., et al. 2002, *A&A*, 393, 821
- Sun, L., Zhou, H., Ji, T., et al. 2017, *ApJ*, 838, 88
- Tombesi, F., Cappi, M., Reeves, J. N., et al. 2010, *A&A*, 521, A57
- Tombesi, F., Meléndez, M., Veilleux, S., et al. 2015, *Nature*, 519, 436
- Vanden Berk, D. E., Richards, G. T., Bauer, A., et al. 2001, *AJ*, 122, 549
- Veilleux, S., Kim, D.-C., Rupke, D. S. N., et al. 2009, *ApJ*, 701, 587
- Veilleux, S., Meléndez, M., Sturm, E., et al. 2013, *ApJ*, 776, 27
- Veilleux, S., Bolatto, A., Tombesi, F., et al. 2017, *ApJ*, 843, 18
- Véron-Cetty, M.-P., Joly, M., & Véron, P. 2004, *A&A*, 417, 515
- Wang, H., Wang, T., Zhou, H., et al. 2011, *ApJ*, 738, 85
- Welty, D. E., Hobbs, L. M., Lauroesch, J. T., et al. 1999, *ApJS*, 124, 465
- White, R. L., Becker, R. H., Helfand, D. J., & Gregg, M. D. 1997, *ApJ*, 475, 479
- Wilson, J. C., Henderson, C. P., Herter, T. L., et al. 2004, *Proc. SPIE*, 5492, 1295
- Wright, E. L., Eisenhardt, P. R. M., Mainzer, A. K., et al. 2010, *AJ*, 140, 1868

- Xiao, T., Wang, T., Wang, H., et al. 2012, MNRAS, 421, 486
- York, D. G., Adelman, J., Anderson, J. E., Jr., et al. 2000, AJ, 120, 1579
- Zafar, T., Møller, P., Watson, D., et al. 2015, A&A, 584, A100
- Zhang, K., Dong, X.-B., Wang, T.-G., & Gaskell, C. M. 2011, ApJ, 737, 71
- Zhang, S., Zhou, H., Shi, X., et al. 2017, ApJ, 845, 126
- Zheng, X. Z., Xia, X. Y., Mao, S., Wu, H., & Deng, Z. G. 2002, AJ, 124, 18

Table 1. Photometric and Spectroscopic Observations

Band	Magnitude Flux [mag Jy]	Survey/Telescope	Obs. Date (UT)	Ref.
Photometries				
u(PSF)	$21.25 \pm 0.10$ mag	SDSS	2004 Apr 16	1,2
g(PSF)	$19.02 \pm 0.02$ mag	SDSS	2004 Apr 16	1,2
r(PSF)	$17.21 \pm 0.01$ mag	SDSS	2004 Apr 16	1,2
i(PSF)	$16.11 \pm 0.02$ mag	SDSS	2004 Apr 16	1,2
z(PSF)	$15.84 \pm 0.02$ mag	SDSS	2004 Apr 16	1,2
<i>J</i>	$14.08 \pm 0.03$ mag	2MASS	2000 Jan 02	3
<i>H</i>	$12.91 \pm 0.03$ mag	2MASS	2000 Jan 02	3
<i>K<sub>s</sub></i>	$11.60 \pm 0.02$ mag	2MASS	2000 Jan 02	3
<i>W1</i>	$9.92 \pm 0.01$ mag	<i>WISE</i>	2010 May 23	4
<i>W2</i>	$8.84 \pm 0.01$ mag	<i>WISE</i>	2010 May 23	4
<i>W3</i>	$6.17 \pm 0.01$ mag	<i>WISE</i>	2010 May 23	4
<i>W4</i>	$3.63 \pm 0.01$ mag	<i>WISE</i>	2010 May 23	4
25 $\mu$ m	$0.348 \pm 0.022$ Jy	IRAS	1983	5
60 $\mu$ m	$1.59 \pm 0.18$ Jy	IRAS	1983	5
100 $\mu$ m	$1.52 \pm 0.17$ Jy	IRAS	1983	5
850 $\mu$ m	$5.6 \pm 1.9$ mJy	SCUBA	2003 Jan 18	6
1.4GHz	$106.07 \pm 0.12$ mJy	<i>FIRST</i>	1994 Jun 14	7
Spectroscopies				
3610–10390 [Å]	...	SDSS/BOSS	2013 Mar 16	8
9800–24500 [Å]	...	P200/TSpec	2013 Feb 24	This Work
9000–20790 [Å]	...	VLT/ISAAC	2013 Mar 20	9
4.4–38.2[ $\mu$ m]	...	Spitzer/IRS	2004-May-11	10

References. — (1) York et al. 2000; (2) Abazajian et al. 2009; (3) Skrutskie et al. 2006; (4) Wright et al. 2010; (5) Moshir & et al. 1990; (6) Clements et al. 2010; (7) White et al. 1997; (8) Ahn et al. (2014); (9) ESO program: 088.B-0997(A); (10) Higdon et al. 2006, reduced data: Leboutteiller et al. 2011;

Table 2. Emission Line Components

Component	$v_0^{(a)}$ km s <sup>-1</sup>	$FWHM$ km s <sup>-1</sup>	Line Profile
Fe II BEL	10±20	1800±200	Lorentzian
Fe II NEL	120±10	740± 50	Gaussian
NEL	0±10	570± 40	Gaussian
Pa $\alpha$ <sup>(b)</sup>	0±10	890± 50	...
Pa $\beta$ <sup>(b)</sup>	0±30	1100±300	...
H $\alpha$ <sup>(b)</sup>	-70± 10	1310± 40	...
H $\beta$ <sup>(b)</sup>	-130±20	1450±130	...

Note. —

(a) Relative velocity in the quasar’s rest frame,  $z = 0.18966$ .

(b) Centroids and  $FWHM$ s of FeII multiplets are derived from model parameters, centroids and  $FWHM$ s of H $\alpha$  , H $\beta$  , Pa $\alpha$  , Pa $\beta$  emission lines are directly measured.

Table 3. Outflow Emission Line Properties

Transition	Flux <sub>Fast</sub> OEL 10 <sup>-17</sup> erg s <sup>-1</sup> cm <sup>-2</sup>	Flux <sub>Slow</sub> OEL 10 <sup>-17</sup> erg s <sup>-1</sup> cm <sup>-2</sup>	Average Velocity $\bar{v}^{(a)}$ km s <sup>-1</sup>
[O III] $\lambda$ 5007	650±90	1230±80	-1330
H $\beta$	110±90	110±60	-1640
[O II] $\lambda$ 3727	20±10	170±30	-810
[Ne III] $\lambda$ 3869	65±40	>90	-1200
[Ne III] $\lambda$ 3968	50±30	60±30	-1420
[Ne V] $\lambda$ 3427	30±20	70±20	-1260
[Ne III] $\lambda$ 15.56 $\mu$ m	500±400	1700±200	-960
[Ne V] $\lambda$ 14.32 $\mu$ m	600±500	1000±300	-810

Note. —

(a). Flux weighted relative velocity in the quasar’s rest-frame.